OPTO-MECHANICAL INTERACTIONS : FROM SENSING TO SYNCHRONIZATION

A Dissertation

Presented to the Faculty of the Graduate School

of Cornell University

in Partial Fulfillment of the Requirements for the Degree of

Doctor of Philosophy

by

Shreyas Yogesh Shah

February 2016

OPTO-MECHANICAL INTERACTIONS : FROM SENSING TO SYNCHRONIZATION

Shreyas Yogesh Shah, Ph.D.

Cornell University 2016

High-quality-factor optical microresonators have emerged as a verstatile tool in studying light-matter interactions and their technological applications. They have proven to be particularly efficient sensors by transducing weak interactions, such as a minuscule change in effective refractive index, into a large optical output signal, when interrogated near their resonance frequencies. Their large quality factors and small sizes also lead to a build-up of large optical forces within the devices. These forces are a driver of high-quality mechanical oscillations of the optical resonator.

The resolution of accelerometers is limited by fundamental thermomechanical noise and by extra noise added by the readout mechanism. We present a platform based on SiN optical microresonators with a high quality factor (Q), which can be used as highly sensitive displacement sensors to minimise readout noise in accelerometers. In addition, we demonstrate integration of SiN micromechanical resonators, which also potentially demonstrate very high quality factors, with a large micromachined mass, which can be used to lower thermomechanical noise in accelerometers. The SiN ring resonator with the SiN micromechanical resonators together can potentially measure acceleration with nano-g resolution over a broad bandwidth.

Frequency-locking between mechanical oscillators is of scientific and technological importance. However, existing schemes to observe such behaviour are not scalable over distance. We demonstrate a scheme to couple two independent mechanical oscillators, separated in frequency by 80 kHz and situated far from each other (3.2 km), via their

optomechanical interactions. Using light as the coupling medium enables this scheme to have low loss and be extended over long distances.

Delay-coupled oscillators exhibit unique phenomena that are not present in systems without delayed coupling. We experimentally demonstrate mutual synchronisation of two free-running micromechanical oscillators, coupled via light with a total delay 139 ns (approximately four and a half times the mechanical oscillation time period). This coupling delay induces multiple stable states of synchronised oscillations, each with a different oscillation frequency. These states can be accessed by varying the coupling strengths. This result could enable applications in reconfigurable radio-frequency networks, and novel computing concepts.

BIOGRAPHICAL SKETCH

Shreyas Shah was born on August 2nd, 1986 in Bombay, India. He spent his childhood in idyllic suburban Bombay, playing cricket and badminton in the streets and sketching and reading indoors on hot (or rainy) Indian afternoons. His initial interests in history, literature and writing were soon overtaken by science, due to an inspiring high-school science teacher. This, along with encouragement from his parents, nudged him towards signing up for preparatory classes for the formidable entrance exam for the Indian Institutes of Technology. This would lay the groundwork for his scientific education.

This period is also seeded his interest and inclinication towards scientific analysis and research. After joining IIT Bombay in the Dual Degree programme (5 year integrated Bachelor of Technology and Master of Technology) in Electrical Engineering, specialising in Microelectronics, he sought out every possible opportunity to further his scientific knowledge. This early involvement led him to an undergraduate journal club, where he first learnt about nanotechnolgy, carbon nano-materials, cosmology, spintronics, etc. He spent summers on campus, volunteering in labs, learning about microfabrication and nanofabrication processes. He also got an opportunity to spend a summer in the lab of Prof. Sanjay Krishna at the Center for High Technology Materials at the University of New Mexico, learning about self-assembled semiconductor quantum dots and IR detectors.

He continued studying self-assembled quantum dots with Prof. Subhananda Chakrabarti for his master's research at IIT Bombay, focussing on relating material properties to their optoelectronic characteristics. Around this time, he also took classes with a visiting professor, Dr. Benjamin G. Lee, on optoelectronics and photonics. This also gave a direction to his research interests as he began applying to Ph.D. programmes in the US.

He graduated with a B.Tech. and an M.Tech. from IIT Bombay in August 2010 and joined Prof. Michal Lipson's lab at Cornell University. The rest, is summarised as contents of this dissertation.

Dedicated to my parents and Ash

ACKNOWLEDGEMENTS

The foremost note of thanks goes to my advisor, Prof. Michal Lipson, for giving me the opportunity to work amongst some of the leading scientists, at the cutting edge of the field. Her mentorship, and nurturing of a 'playground' of sorts for young trainee scientists, have played an pivotal role in my growth, both as a person and as a scientist. The growth process hasn't always been straightforward, or easy, but her persistence and foresight is one of the main reasons I am able to see the finish-line of this academic marathon.

I would also like to thank my committee members, Prof. Richard Rand, Prof. Alexander Gaeta and Prof. Clifford Pollock for providing me valuable feedback different junctures of my career as a graduate student. I would like to express especial appreciation towards Prof. Rand. Our weekly meetings discussing nonlinear dynamical problems and trying to make headway into some of the theoretical problems I faced in my research taught me not only about that field, but also helped me make connections between theoretical analysis its role and limitations vis-a-vis experimental work.

Of course, a lot of the daily guidance came from the senior scientists in the lab - Carl Poitras and Jaime Cardenas. As much as Michal set the direction of research, Carl and Jaime helped in getting me off the ground, especially as a new student, and later when my research hit roadblocks. I owe a lot to their calming influence not only in my own life as a graduate student, but also in the lab, enabling a great work environment. Mohammad Soltani and Gustavo Wiederhecker were, by far, my biggest inspirations during the period when I overlapped with them. The depth of their expertise, their resourcefulness and their energy and enthusiasm were infectious. I appreciate having known them and worked with them, and certainly, having learnt a lot from them. Raphael St-Gelais was incredibly helpful with valuable feedback, especially during the last stage of my research, which overlapped with his expertise.

Interactions with Amin and Felippe always felt more like those with a friend or a senior colleague, than those with a purported post-doc. My especial thanks goes to Felippe who worked with me during the last stages of my research, and helped me make sure of my sanity, or insanity, as the case may be, during the roller-coaster that the accelerometer project was.

These five-odd years were spent with my comrades-in-arms - Mian, Danny, Lawrence, Austin, Kevin, Vishal. The relationships we've built while taking over the lab, I feel, go beyond the lab, and I hope to cherish your friendship well into my old age. I have learnt from you, perhaps more outside the lab than inside. I cannot think of a better cohort with which to go on this journey towards a Ph.D. Indeed, there were others who joined before as well as after us, who were as much a part of this circle. Avik, Aseema, Chris, Steven, Romy have provided more than enough memories and lessons to perhaps constitute a separate Ph.D. journey in itself.

I would also like to express gratitude towards the senior graduate students in the lab - Kyle, Art, Nick, Jake, Hugo, Lucas, Lian and Bishu - from whom we not only learnt, but inherited a lab, and research practices, that laid the foundation of this journey. I hope that as I and my cohort leaves, we have done the same with the newcomers - Brian Stern, Moshe, Gaurang, Ipshita, William, Brian Lee and the new folks who joined at Columbia University.

None of this would be possible without the funding agencies that sponsor most of the research in this lab, as well as my own research and tuition.

I also thank my parents for continuing to support me, in spirit and with constant words of encouragement. Lastly, but certainly not in the least, I owe this success to Ashwana (Ash). She has been my pillar of strength, a well of support and encouragement, and a confidant and friend who has helped me through some of the toughest times I've experienced.

TABLE OF CONTENTS

LIST OF FIGURES

CHAPTER 1

INTRODUCTION

1.1 Light-matter interaction

Interaction between electromagnetic fields and matter is an essential aspect of the physical world, as well as human culture and technology. Rainbows, for example, are formed because different colours of white light interact with air differently and propagate at different speeds, causing them separate. A microwave oven heats water by exciting its molecular motion through radio-frequency electromagnetic radiation. Even cosmic features, such as the long tails of comets, are a result of light from the sun pushing on the dust and gas surrounding such objects. From paints and pigments that have provided colour to works of art since ancient times, to modern technology like lasers, these fundamental interactions are all-pervasive.

Such interactions can be summarised by considering the response of charged particles in matter to an external electric field. These particles may be freely moving electrons in metals and similar materials, bound electrons in atoms or atomic crystals, or ions. Displacement of these charged particles due to the electric field results in a net dipole moment in the body. As a result, the electric field experiences a modified dielectric constant Eq. 1.1 [71], where ω is frequency of the applied electric field, and χ_e, the dielectric susceptibility. In general, this change in the dielectric contant not only changes the effective speed of light as it interacts with that material, but also decreases (or increases!) its intensity as it propagates.

$$\epsilon(\omega) = 1 + \chi_e(\omega) \tag{1.1}$$

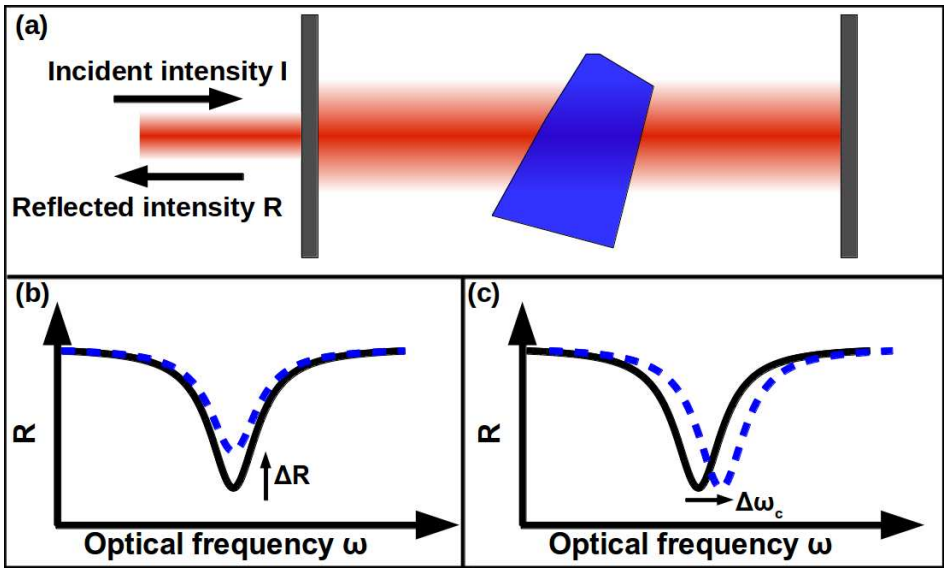

Figure 1.1: **(a)** Schematic of a cavity formed by two mirrors. As light with frequency equal to resonance frequency ω_c is confined between the two mirrors, it interacts with the perturbing matter more strongly. **(b)** If the perturbation is merely in the intensity of light, it increases the intensit of light reflected at resonance. **(c)** If the object affects the speed of light, it changes the resonance frequency.

1.2 Sensing using optical cavities

The effect that light-matter interactions have on the intensity and the speed of light, via the modified dielectric constant $\epsilon(\omega)$, can be used in a variety of sensing applications. However, typical interactions of light with matter, especially with very small objects such as atoms, perturb its intensity or speed only slightly [8]. Therefore, any measurable change only occurs when light interacts with the source of perturbation over long propagation distances [34], or for a long duration. Optical cavities have the ability to confine light in a small region for long periods time (relative to the time it would take to travel the same distance as the length of the cavity). Any perturbation of light taking place in the cavity, therefore, is enhanced as light interacts for a longer period over a greater effective distance, with the perturbing medium.

The enhanced interaction in optical cavities occurs near characteristic 'resonance' frequencies of the cavity. This 'resonant-enhancement' is best understood by looking at the effect that perturbations have on the light coming out of the cavity (canonically represented by two mirrors, Fig. 1.1, forming a Fabry Perot resonator [40]). If the interaction attenuates the intensity of light in the cavity, it increases the intensity of light reflected from the cavity. If the interaction perturbs the speed of light in the cavity, it results in a change in the resonance frequency. Resonant-enhancement is higher for a low loss (high quality factor, Q) cavity [14].

Resonant-enhancement in high-Q optical cavities has proven to be useful in biological and chemical sensing applications [7, 33] to probe materials which absorb light very weakly [72], or even single molecules [8] and viruses [101]. It has also shown unprecedented sensitivity in interrogating mechanical motion for displacement sensors [38], accelerometers [57, 56] and even quantum-limited motion of microscopic structures [6].

1.3 Optical forces

Electromagnetic fields also have a well-defined momentum associated with them [71]. Therefore, electromagnetic radiation exerts a pressure, proportional to its intensity, on any physical surface on which it is incident. In other words, photons incident on a body impart a momentum change, and thereby a force, on that body. In addition to this 'radiation pressure', spatial variations in the electromagnetic field acting on a polarizable body induce a 'dipole-force', which is proportional to the gradient of the intensity of electric and magnetic fields, and the polarizability of the body. These forces are summarized in Fig. 1.1.

The most prominent application of optical forces is the technique developed by

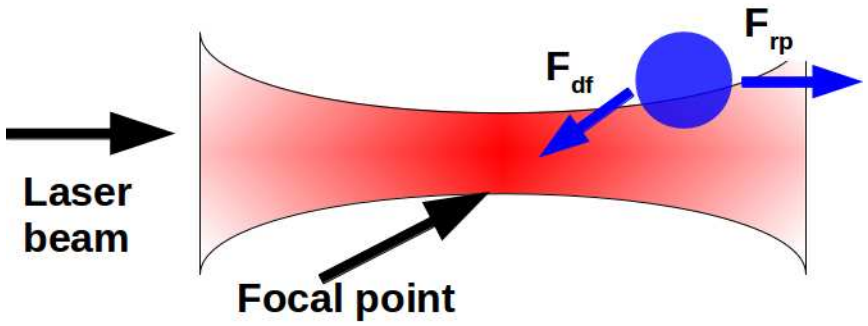

Figure 1.2: An object near the focal point of a focussed laser beam experiences a dipole-force F_{df} towards the focus, and a radiation pressure force F_{rp} along the direction of propagation of the laser beam

Arthur Ashkin and others to trap and manipulate microscopic particles using a tightly focussed laser beam [9]. This technique makes use of both, radiation pressure and the strong dipole force created by the large gradients to hold a particle near the focal point of the laser beam. Such strong gradients are also present in the vicinity of optical waveguides which tightly confine electric field [4], and can be used to trap microparticles [85] for optofluidic and lab-on-chip applications [91]. In addition, these gradient optical forces can also be used to make tunabe optical couplers [35] and resonators [102].

1.3.1 Cavity optomechanics

Of particular interest is the role of electromagnetically induced forces in optical resonators, such that physical boundaries of the optical cavity are deformed under the influence of these forces. These 'optomechanical' interactions first attracted attention within the field of gravitational-wave detection via optical interferometers. These interferometers consist of massive mirrors which are mounted movable platforms and which are expected to move due to theoretically predicted gravitational fluctuations. As described in the previous section, optical cavities are particularly efficient at detecting mechanical

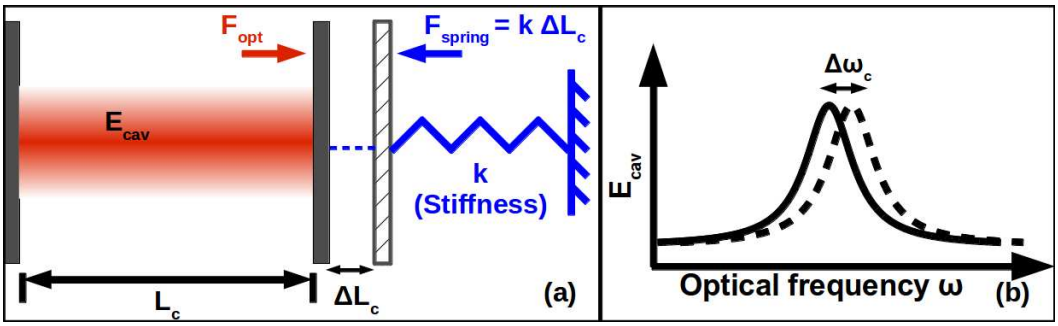

Figure 1.3: **(a)** An optomechanical resonator, schematically depicted as a Fabry-Perot cavity. One mirror forming the cavity can move under the opposing forces F_{opt} and F_{spring}. Motion of the mirror changes the length of the cavity L_c, and thereby it's resonance frequency ω_c. **(b)** Change in L_c causes a change in ω_c, and the energy in the cavity E_{cav}.

motion. However, the presence of optical forces imposes a lower bound on the detection of fluctuations in gravitational forces, since both types of forces have the same effect on the movable mirror.

Canonically, such an optical cavity may be represented by a Fabry-Perot Cavity (Fig. 1.3), where one mirror is fixed, and the other mirror is mounted on a spring. It is evident that radiation pressure on this movable mirror can change the length of the cavity L_c, and thereby affect the characteristic frequencies ω_c of the optical resonator. The strength of this interaction is described by the optomechanical coupling coefficient G_{om}, which influences not only ω_c, but also the force F_{opt} acting on the mirror (Eq. 1.2).

$$\begin{aligned} \Delta\omega_c &= G_{\mathrm{om}} \times \Delta L_c \\ \frac{F_{opt}}{M} &\propto \frac{G_{\mathrm{om}} E_{cav}}{M}, \\ \text{where, } E_{cav} &= \text{Optical energy in the cavity} \\ \text{and, } M &= \text{Mass of the mirror} \end{aligned} \tag{1.2}$$

The optical energy E_{cav}, and thereby the force on the mirror, depends on the

frequency-detuning between the resonator and the laser probing it (Eq. 1.2), which is, in turn, affected by the position of the mirror. This interdepedence, termed 'backaction', has several significant consequences.

Static Backaction

The presence of an additional position-dependent force on the mirror-spring system modifies the effective spring constant [88] (the 'optical-spring' effect). Therefore, the mechanical frequency of the mirror-spring system either increases or decreases, depending on whether the initial frequency detuning is positive or negative [88]. In optomechanical systems engineered to have an especially strong backaction, [29], F_{opt} can be as large as the force of the spring itself, resulting in a hundred-percent change in the effective mechanical frequency!

In addition, it must be pointed out that the interaction between the optical resonator and the mechanical resonator formed by the mass-spring system is essentially nonlinear. As a result, this 'optomechanical resonator' is bistable [28] i.e. there exist two well-defined positions of the mirror where the force of the spring exactly balances the optical force. This is in contrast to the behaviour of a simple mass-spring system, which linear and has a single stable position under the influence of a constant force.

Dynamical Backaction

The optical force F_{opt} influences not only the position of the mirror, but also its velocity. This is due to the fact that optical cavities have a finite response-time i.e. for any given change in the position of the mirror, E_{cav} reaches a steady state value corresponding to the new position, at a rate equal to the optical damping of the cavity. Therefore, there

is always a time-lag between change in E_{cav} (and thereby F_{opt}) and the position of the mirror. This results in there being net work done by F_{opt} on the mass-spring system.

Just like the optical-spring effect, this 'dynamical backaction' has drastically different effects when the frequency detuning between the optical cavity and the laser is positive and negative. For negative detuning, F_{opt} does a net negative work on the mass spring system i.e it takes mechanical energy out of the mass-spring system. This increases the effective mechanical damping. On the hand, for positive detuning, F_{opt} reduces the effective mechanical damping, and amplifies the mechanical motional amplitude.

If the dynamical backaction is strong enough at positive detuning, the positive work done on the mirror can overcome mechanical losses, giving rise to self-regenerating mechanical motion. This transition from damped mechanical motion to self-sustained oscillations is akin to the onset of lasing in optical cavities with optical gain.

1.3.2 Micro-optomechanical oscillators

The effect of backaction is larger in optomechanical resonators with a lighter mechanical element. Therefore, micromechanical resonators, with effective masses in the range of femto-grams [95] to nanograms [84], have emerged as a especially attractive platform to study optomechanical effects [54]. Micromechanical resonators are a technologically important platform, and are widely used as sensors [15], tunable electronic and optical devices [113, 104], as well as in (RF) communications [31]. In particular, optically-induced self-sustained oscillations of micromechanical resonators, which naturally vibrate at radio frequencies (RF) i.e. in the kilo-Hertz to giga-Hertz range, are a natural interface between the RF and the optical domain.

Micro-optomechanical oscillators are generators of high-quality, single-tone RF signals [80]. At room temperature, the spectral spread i.e. the linewidth of these oscillation signal is only limited by random phase fluctuations due to interaction of the mechanical resonator with the surroundings [81]. Therefore, these oscillators can be used to provide low-noise frequency reference [79, 64] as well as to down-convert and detect RF signals [44] carried by optical frequencies. In addition, the nature of optomechanical interactions makes it possible to directly, coherently and efficiently convert signal carried by optical frequencies to the RF domain, and vice-versa [13, 36, 5, 10]. Micro-optomechanical oscillators, therefore, are an ideal platform for RF-photonic communication, with potential for even quantum information processing [13].

1.4 This dissertation

In this dissertation, we will touch upon the two broad aspects of light matter interactions in optical cavities mentioned above viz. sensing, and optomechanical oscillators.

Chapter 2 describes nanophotonic platform consisting of low-loss optical and mechanical resonators that can be used to sense displacement and acceleration with a high-resolution.

Chapters 3 presents a scheme to couple two physically distant optomechanical oscillators solely via optical interactions. The RF oscillations of one oscillator modulate the optical force on the other oscillator, causing it to be frequency-locked. This optically-induced frequency locking has applications in RF communication networks.

Chapter 4 shows that the propagation delay in coupling two optomechanical oscillators via optical interactions causes the two oscillators to synchronise at one of multiple

possible frequencies. This behaviour is reminiscent of networks of biological oscillators, and as such, can be used as a platform for information processing inspired by neural oscillators.

CHAPTER 2

SILICON-NITRIDE-BASED NANOPHOTONIC PLATFORM FOR BROADBAND NANO-G ACCELERATION SENSING

Optical readout of mechanical motion in sensors like accelerometers [19, 20, 37, 56, 57, 109] enables measurement with unprecedented resolution [20, 37, 56, 57] over a broad bandwidth [20, 37, 56]. However, previously demonstrated broadband optical accelerometers are limited in their resolution to μg levels, and nano-g level resolution is only possible at very low frequencies [57]. Acceleration resolution $a_{min} = \sqrt{(a_{th}^2 + a_{RO}^2)}$ is limited by thermomechanical noise a_{th}, and by the noise-equivalent-acceleration (NEA) a_{RO} added by optical readout of mechanical motion. a_{th} can be reduced by increasing the mass displaced upon acceleration, and reducing mechanical dissipation (A.5). a_{RO} can be reduced by improving the sensitivity of transduction of mechanical displacement. A higher displacement sensitivity also enables acceleration sensing with a higher resolution at higher frequencies (A.3) [57].

Silicon nitride, which is widely used in nanophotonics as a platform for optical communication [89], nonlinear optics [61] and cavity optomechanics [30], can be used to make high-Q microresonators, such as ring resonators [66] and microdisks [87], for highly sensitive transduction of mechanical motion. SiN has also been used to demonstrate high-Q micromechanical resonators (nanotethers) [100]. Its compatibility with standard micromachining processes [46] enables integration of a large mass with the nanotethers in order to reduce thermomechanical noise.

In this chapter, we present a silicon-nitride based platform, consisting of a high-Q SiN ring resonator that can detect the displacement of an SiN membrane with fm-level

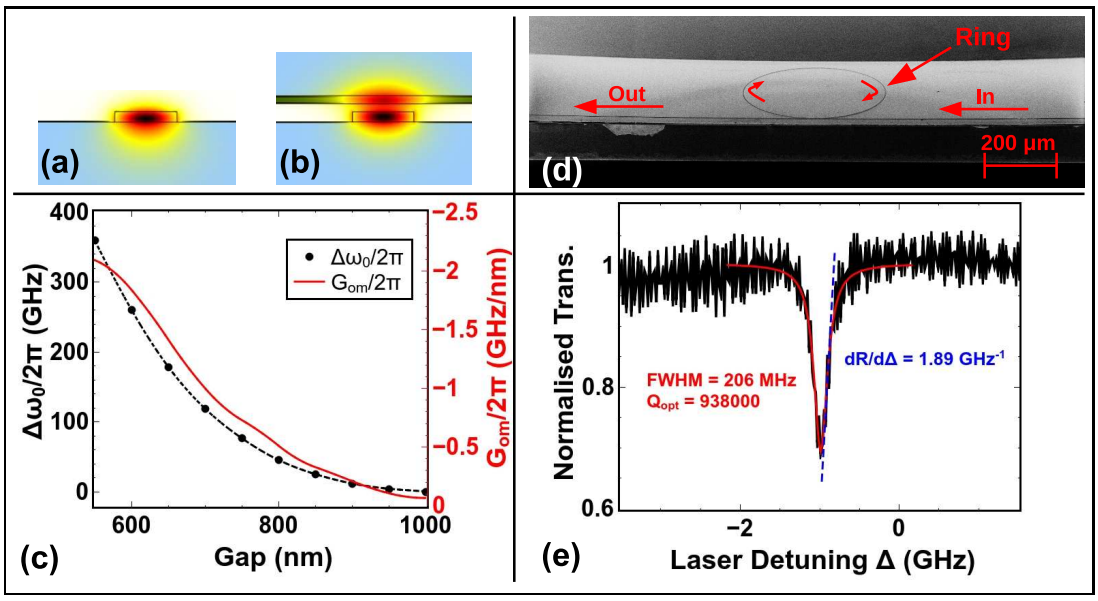

Figure 2.1: **(a)** Schematic depiction of the cross-sectional profile of the optical mode confined in the SiN ring resonator. **(b)** When the SiN membrane is brought close to the resonator, the optical mode profile now includes a significant overlap with the membrane, changing the effective index of the mode, and thereby the resonance frequency. **(c)** The resonance frequency ω_0 changes by $2\pi\times360$ GHz as the gap between the ring and the SiN membrane is reduced from 1 μm to 550 nm, with a maximum rate of change $\frac{d\omega_0}{dx} = -2\pi \times 2$ GHz/nm **(d)** SEM image of the ring resonator and bus waveguide. The image was taken with the sample tilted by 70 degrees. **(e)** Normalised optical transmission of the ring resonator, showing the high-Q resonance dip. A Lorentzian-curve-fit yields a linewidth of $2\pi \times 206$ MHz, and a steep slope $\frac{dR}{d\omega_0} = \frac{1}{2\pi} \times 1.89$ GHz^{-1}.

resolution, and thereby enable ultra-low a_{RO}. The presence of the SiN membrane perturbs the optical mode of the waveguide forming the ring resonator and influences the effective refractive index of the mode. This, in turn, changes the optical resonance frequency ω_0. Mechanical displacement of the membrane, therefore, is tranduced into a change in the resonance frequency with a sensitivity $G_{\text{om}} = \frac{d\omega_0}{dx}$, where 'x' is the position of the membrane relative to the ring. When the ring is pumped with a laser with a frequency slightly off resonance, a shift in resonance frequency causes a change in the transmitted power R. For a high-quality resonator, the sensitivity of R to changes in

ω_0 (i.e. $\frac{dR}{d\omega_0}$) is high. We demonstrate quality factors as high as 938000 for resonances in air-clad SiN rings with 200 μm radius, 1.5 μm width and 330 nm height (Fig. 2.1). These high quality factors are a result of the high optical quality of SiN obtained using low-pressure (LP) chemical vapour deposition (CVD) on a substrate of SiO grown thermally on Si (See A.1). Such a high quality factor gives us $\frac{dR}{d\omega_0}$ as high as $\frac{1}{2\pi} \times 1.89$ GHz^{-1} (Fig. 2.1). The sensitivity G_{om} depends on the separation between the ring and the SiN membrane. The closer the membrane is to the ring, the greater the change in the refractive index for the same amount of displacement. As the gap is reduced from 1 μm to 550 nm, we see (Fig. 2.1), using finite element simulations, G_{om} as high as $2\pi \times 2$ GHz/nm. This high value of G_{om}, together with a high $\frac{dR}{d\omega_0}$, gives us a displacement sensitivity $\frac{dR}{dx}$ of 3.78 nm^{-1}. Assuming 10 μW of laser power at the input and assuming 1% of this power reaches the photodetector, this corresponds to a laser-shot-noise-limited displacement resolution of 4.2 fm/ $\sqrt{\mathrm{Hz}}$ (See A.1).

We show that SiN nanotethers support a large proof mass on an SiN membrane, which, along with ultra-low mechanical damping, is necessary for nano-g levels of a_{th}. A combination of surface- and bulk-micromachining enables us to integrate a 500 μm thick crystalline-Si proof mass on a 200 nm thick SiN membrane, which is suspended by SiN nanotethers which are only 200 nm thick, 10 μm wide and 50 μm long (See A.2, Fig. 2.2). The bandwidth of operation of an accelerator is characterised by the resonance frequency of the mechanical element. The relatively large Young's modulus of SiN (E = 2.5×10^{11} Pa, [110]) can also enable the tether-mass system to have the large resonance frequencies necessary for broadband acceleration sensing. The mechanical frequency, therefore, can be designed by adjusting the dimensions of the tethers (Fig. 2.2) (See A.3), without compromising on the proof-mass and hence, a_{th}. Therefore, for a typical 420 μm x 300 μm proof mass fabricated in this manner, with a mass of 150 μg, a mechanical resonance frequency of 2 kHz, and assuming a mechanical quality factor of

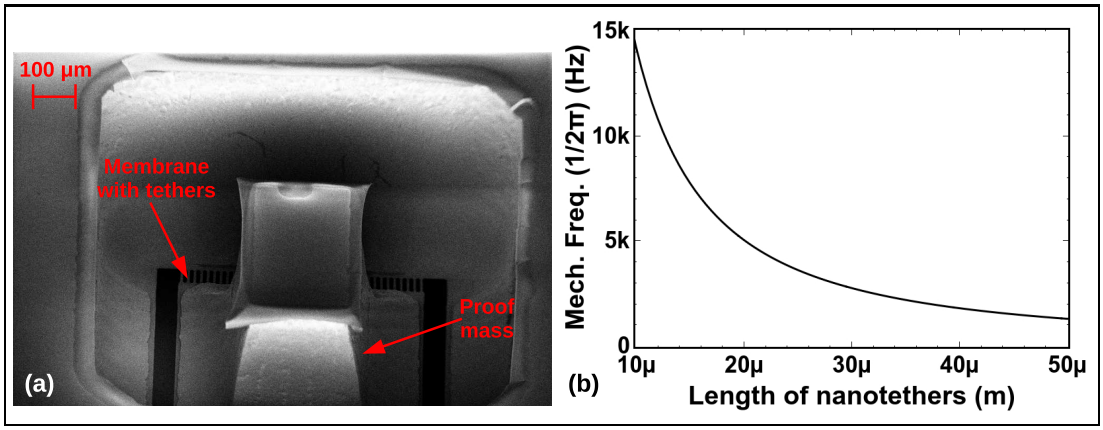

Figure 2.2: **(a)** SEM image of a typical proof mass fabricated by bulk micromachining of an 500 μm thick Si wafer, and monolithically integrated with a 200 nm thick SiN membrane, suspended by SiN nanotethers with dimensions 200 nm x 10 μm x 50 μm. **(b)** 60 such nanotethers, supporting a 150 μg proof mass can show a mechanical resonance frequency as high as 15 kHz.

10000 [100], we can achieve a_{th} = 38 ng/ $\sqrt{\text{Hz}}$ (See A.1).

The interaction of the high-Q SiN ring resonator with the SiN membrane, enables acceleration sensing with nano-g resolution, limited only by the fundamental thermo-mechanical noise a_{th}. In order to take full advantage of the high mechanical quality SiN nanotethers and the large proof-mass, it is necessary to reduce the extra noise added due to 1) the optical noise in the laser (which is fundamentally limited by optical shot noise a_{SN}), and 2) the electronic noFiguresise in the photodetector a_{det}, where, $a_{\text{RO}}^2 = a_{\text{SN}}^2 + a_{\text{det}}^2$. This is achieved by optically enhancing the transduction of mechanical motion of the SiN membrane, by a factor $G_{\text{om}} \frac{dR}{d\omega_0}$. The noise sources contributing to a_{RO} do not experience the same amplification (See A.1). For example, a laser power of 10 μW corresponds to a shot noise of 1.6 pW/ $\sqrt{\text{Hz}}$, but only contributes 4.2 ng/ $\sqrt{\text{Hz}}$ to the NEA. Similarly, a typical photodetector (See A.1), with a noise-equivalent-power of

0.6 pW/ $\sqrt{\text{Hz}}$, only adds 1.6 ng/ $\sqrt{\text{Hz}}$, thereby leaving a_{th} as the dominant, and limiting, noise factor in sensing acceleration.

The strength of interaction i.e. the value of G_{om},strongly depends on how parallel the surface of the ring and the membrane are, but any detrimental effects due to misalignment between the two surfaces are mitigated due to the high quality factor of the SiN ring resonator. We show that the G_{om} is $-2\pi \times 2.1$ MHz/nm when the two substrates of the ring resonator and the SiN membrane are crudely aligned using manual micropositioning stages (Fig. 2.3). Despite the value of Gom being lower than its potential, a high quality factor (938000) ensures that this platform can give $a_{min} = 4.1$ μg/ $\sqrt{\text{Hz}}$ (limited by a_{RO}), which is already comparable to state-of-the-art demonstrations [37, 56]. Advanced packaging techniques can be used to achieve better alignment to improve the G_{om}, as well as to minimise mechanical dissipation caused by viscous drag [99] by creating a hermetic seal around the assembly.

In conclusion, we demonstrate that SiN can be used to make an optical resonator with a quality factor that is high enough for broadband, nano-g level acceleration sensing, limited only by fundamental thermomechanical noise. In addition, we demonstrate that SiN nanotethers can be used to suppport a membrane with the large proof mass necessary in order to achieve nano-g leves of ath. Advanced packaging techniques can be used to achieve sensing performance that is better than current state-of-the-art.

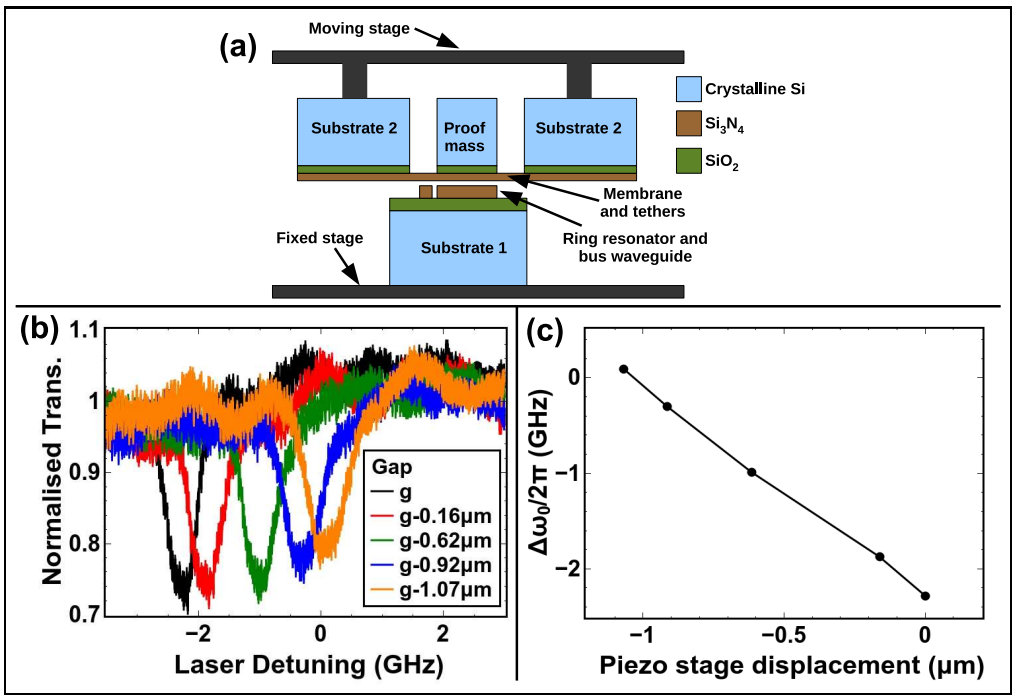

Figure 2.3: **(a)** Schematic depiction of the experimental setup to demonstrate the effect of the interaction between the ring resonator and the membrane. The ring resonator is mounted on a fixed platform. The substrate with the membrane is mounted on a movable stage directly above the ring resonator. A piezo actuator is used to control the height of this stage, and the tilt of the membrane with respect to the ring resonator is minimised, via visual inspection, using manually operated, three-axis tilt micromanipulators. **(b)**, **(c)** Starting from a gap 'g', as the piezo-actuated stage is lowered by 1.07 μm, the resonance frequency increases by $2\pi\times$ 2.3 GHz, giving an average $G_{\rm om} = 2\pi\times 2.1$ GHz/nm. It must be pointed out that due to mutual tilt, one corner of the movable substrate touches the fixed substrate, and pivots around that point of contact as the piezo stage is lowered. As a result, the $G_{\rm om}$ calculated in **(c)** underestimates the actual $G_{\rm om}$ in this setup.

CHAPTER 3

MASTER-SLAVE LOCKING OF OPTOMECHANICAL OSCILLATORS OVER A LONG DISTANCE

Frequency-locking between micromechanical oscillators is critical for RF communication and signal-processing applications [94, 17, 93]; however its scalability is limited by the fact that, in general, the oscillators are obliged to be in physical proximity in order to interact. Micromechanical oscillators can interact at the micron-scale via electronic coupling [70] or a physical connection [90]. However, these schemes are fundamentally lossy over long distances, and therefore, are not scalable. Scaling up coupled mechanical oscillators to macro-scale networks [98, 65, 41] could potentially enable novel concepts in memory and computation [68, 12, 43], as well as provide a platform to put in practice many theories of nonlinear dynamics of coupled oscillators [50, 75].

Interaction of mechanical oscillators through light could, in principle, help overcome this limitation, since light can propagate over long distances with minimal loss. Recent reports [112, 11, 90] on frequency-locking between mechanical oscillators demonstrate interaction only over a few micrometers. In demonstrations of light-mediated coupling of two micromechanical oscillators [112, 11], both mechanical oscillators are coupled to the same optical cavity, limiting the kind of network topologies that can be used and how far the oscillators can be separated.

We demonstrate a reconfigurable scheme to couple, via light, two independent micromechanical oscillators separated from each other by an effective path of 3.2 km, in the master-slave configuration and show the ability to lock their oscillation frequencies. This coupling scheme is based on using light to send the information of the mechanical oscillations from the master oscillator to the slave oscillator. It is facilitated by the fact that each oscillator is an an optomechanical oscillator (OMO), consisting of co-localised

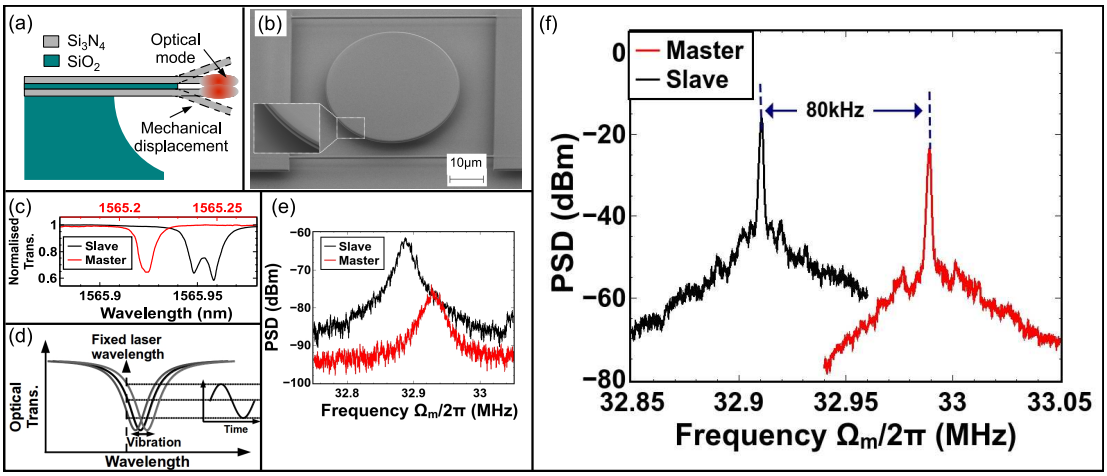

Figure 3.1: **(a)** Schematic depiction of cross-section of the device, indicating the co-localisation of optical and mechanical resonances. The dotted line indicates the relative mechanical displacement between the two disks that influences the optical mode. **(b)** SEM image of the OM resonator. **(Inset)** Higher-magnification SEM image of the region highlighted, showing the double-microdisk structure. **(c)** Normalised transmission spectra of master and slave optical resonances. **(d)** Vibration of the mechanical resonator causes the optical resonance to vibrate about a mean value, resulting in modulation of transmitted optical power **(e)** Power spectral density (PSD) of the modulation of the transmitted optical power due to thermally-induced mechanical vibration shows the natural frequency of the mechanical resonator. **(f)** PSD of master and slave oscillations. The oscillation peaks are offset by 80 kHz.

optical resonances and mechanical resonances that are coupled to each other (Eqs. 3.1, 3.2) [55]. The mechanical resonator can be modelled as a damped simple harmonic oscillator with position 'x', effective mass m_{eff}, frequency Ω_m and damping rate Γ_m. It is driven by its interaction with an optical force $F_{opt} = G_{\rm om}\frac{|a|^2}{\omega}$, where $|a|^2$ is the energy in the optical cavity and ω is the laser frequency. $G_{\rm om}$ indicates the strength of the interaction between optics and mechanics. The optical cavity can also be modelled as a damped oscillator, with a position-dependent frequency $(\omega_0 + G_{\rm om}x)$ and damping rate Γ_{opt}, and it is driven with a laser of power $|s|^2$, coupled to the cavity at the rate Γ_{ex}. The force on the mechanical resonator F_{opt} can be controlled by changing the intracavity energy $|a|^2$,which is, in turn, affected by the laser power $|s|^2$. Any modulation of the laser

power therefore couples to the mechanical resonator via the optical force F_{opt} [45].

$$\frac{da}{dt} = i((\omega - \omega_0) - G_{\mathrm{om}}x)a - \Gamma_{opt}a + \sqrt{2\Gamma_{ex}}s \tag{3.1}$$

$$\frac{d^2x}{dt^2} + \Gamma_m\frac{dx}{dt} + \Omega_m^2 x = \frac{F_{opt}[a]}{m_{eff}} \tag{3.2}$$

The OMOs used for this demonstration each consist of two suspended Si_3N_4 microdisks stacked vertically (Figs.3.1(a), (b)). The optical and mechanical resonances under consideration are co-localised along the periphery of the structure. These structures are fabricated using e-beam lithography techniques [112]. The top and bottom Si_3N_4 disks are nominally 250 nm and 220 nm thick and have a radius of 20 μm. These disks are separated from each other by a 170 nm thick SiO_2 sacrificial spacer layer. This stack rests on a 4 μm thick SiO_2 support layer. These layers are partially etched away to release the periphery of these disks. This suspended structure supports optical whispering-gallery modes that are overlap with the edges of the top and bottom disks (Fig.3.1(a)) [112]. The optical resonance frequency of this structure is strongly dependent on the separation between the two disks. Relative motion (represented by Eq. 3.2) between the two disks changes the resonance frequency at the rate of G_{om}=-$2\pi\times$49 GHz/nm, as calculated from finite element simulations [112].

The two devices, when not coupled, oscillate at two distinct mechanical frequencies separated by 80 kHz. In order to characterise the devices, light is coupled into each resonator with a tapered optical fiber. The transmission spectrum of the master OM resonator shows an optical resonance centered at ~1565.22 nm (Fig. 3.1(c)). Similarly, the slave OM resonator has an optical resonance centered at ~1565.95 nm (Fig. 3.1(c)). The splitting in the resonance is due to back-scattering induced lifting of degeneracy between the clockwise and counter-clockwise propagating modes [53]. Thermal motion of the mechanical resonators modulates this transmission spectrum (Fig. 3.1(d)), which can be analysed with a spectrum analyser. The master is observed to have a mechanical

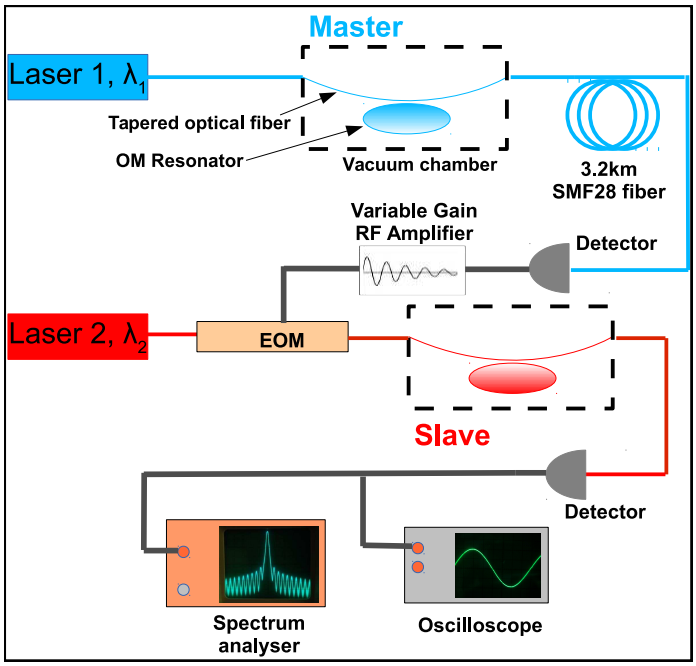

Figure 3.2: Schematic of experimental setup to demonstrate master-slave locking. The two optomechanical (OM) resonators are driven by independent lasers. The optical signal from the master travels through 3.2 km of fiber. The RF signal generated at the detector by the oscillations of the master modulate the laser driving the slave. The RF oscillations of the slave are analysed with a spectrum analyser and an oscilloscope.

resonance at 33.93 MHz (Fig. 3.1(e)), with a linewidth of 16.39 kHz, while the slave has a mechanical resonance centred at 32.82 MHz (Fig. 3.1(e)), with a linewidth of 13.56 kHz. When the optical resonances are excited with blue-detuned lasers ($\omega > \omega_0$), dynamical backaction [55] amplifies mechanical motion. As input power is increased, this mechanical gain increases, until it overcomes intrinsic mechanical damping. At this point, each resonator becomes a self-sustaining oscillator [55]. The master oscillates at 32.99 MHz (Fig. 3.1(f)), and the slave oscillates independently at 32.91 MHz (Fig. 3.1(f)), i.e. separated from the master by more than six times its natural mechanical linewidth. Note that, due to the optical-spring effect [55], the oscillation frequencies for the oscillators are centred at a frequency slightly higher than that for the thermal motion

of the respective resonator.

To demonstrate long-distance locking, we couple the two OMOs in a master-slave configuration, via a 3.2 km long optical fiber, with an electro-optic modulator that is driven by the master OMO and that modulates the laser driving the slave OMO (Fig. 3.2, Eq. 3.3). Each OMO is pumped by an independent laser. The signal transmitted from the master OMO carries information about its position x_{master}. It travels through a 3.2 km long delay line before it is detected with a high-speed detector. The output of this detector carries the radio frequency (RF) oscillations, which are a function of the mechanical displacement x_{master} of the master. The slave laser drive s_{slave} is modulated by this signal from the master (Eq. 3.3). The output of the slave OMO is detected with another high-speed detector and analysed with a spectrum analyser and an oscilloscope.

$$|s_{slave}|^2 = |s_{0,slave}|^2(1 + \gamma[f(x_{master})]) \tag{3.3}$$

The strength of coupling between the slave OMO and the output of the master OMO can be controlled by the modulation depth γ of the electro-optic modulator driven by the master-oscillator. A voltage-controlled variable gain amplifier provides a gain between -26 dB and +35 dB to the RF oscillations coming from the detector of the master OMO, and thereby controls the modulation depth. This is reflected in the power spectral density (PSD) of oscillation peak of the master OMO (H_{inj}) as seen in the light transmitted from the slave OMO (Fig. 3.3).

As we increase the coupling strength, we show that the slave OMO transitions from oscillating independently to being frequency-locked to the master OMO. The coupling strength is determined by comparing the amount of modulation imparted on $|s_{slave}|^2$ by the injected signal and by the slave oscillator. This is measured in terms of the ratio

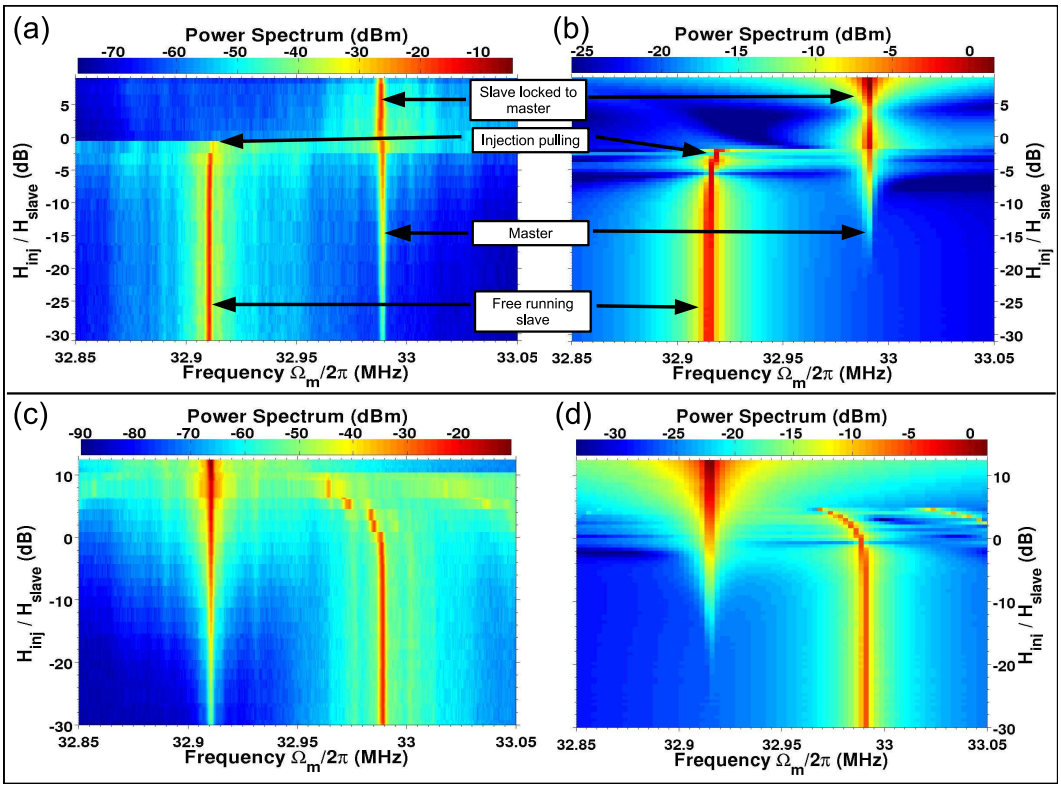

Figure 3.3: **(a)** Spectrum of the power transmitted from the slave OMO for different injection ratios (H_{inj}/H_{slave}). **(b)** Numerical simulation of the power spectrum. **(c)**, **(d)** Same as **(a)** and **(b)**, respectively, only now measured by reversing the roles of master and slave.

of the power of injected oscillation signal (H_{inj}) to the power of the free-running slave oscillation (H_{slave}). When H_{inj}/H_{slave} is small, the slave OMO oscillates at its own frequency, independently. The optical signal transmitted from the slave carries the slave oscillation peak, along with the modulation imparted on the laser (Fig. 3.3(a)). As the injection strength is increased, the slave oscillation frequency is pulled towards the master oscillation frequency. After a transition point ($H_{inj}/H_{slave} \sim$ -2 dB), the slave OMO spontaneously begins oscillating at the same frequency as the master OMO.

We show that frequency locking can also occur when the roles of the slave and the master are reversed (Fig. 3.3(c)). As we increase the coupling strength, the new-slave spontaneously begins oscillating at the same frequency as the new-master after a

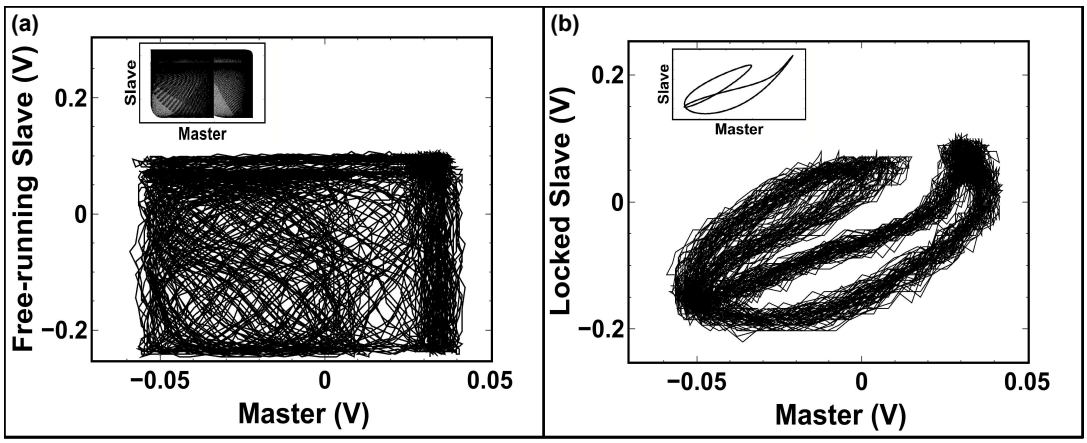

Figure 3.4: Phase-portraits formed by the oscillation signals of the **(a)** free-running slave and **(b)** locked slave with the master oscillator, as measured with an oscilloscope, over more than 130 oscillation cycles.**(Insets)** Simulated phase-portraits

transition point around $H_{inj}/H_{slave} \sim 8$ dB. The difference in the locking strength for each of the oscillators can be attributed to the strongly nonlinear nature of these oscillators ([108], See Appendix B for a theoretical analysis of the locking process, and additional data on locking dynamics.).

We observe phase locking between the master and the slave oscillators when their frequencies lock. The locking-transition is associated with the establishment of a fixed phase-relationship between the master and the slave oscillations. We can observe the change in the phase-relationship upon locking between the master and slave oscillators by plotting the oscillation signal of the slave versus that of the master, over a duration long enough to accommodate phase drift. When the slave OMO is free-running, its phase is uncorrelated to the phase of the master OMO. As a result, for each point in the phase space of the master OMO, the phase of the slave OMO can take any value in its range (i.e. 0^0 to 360^0). This is reflected in the phase-portrait of the oscillations of the master OMO and slave OMO forming a filled-rectangle (Fig. 3.4(a)), over an extended period of time (4 μs, i.e. more than 130 oscillation cycles) [74]. When the slave

OMO is locked to the master OMO, the phase difference between the two oscillations is fixed, and the phase-perturbations (phase-noise) are correlated (See Appendix B). This correlation between the phases of the two oscillators results in the X-Y trace of the oscillations (Fig. 3.4(b)) of the master and slave OMOs forming an open Lissajous figure [74].

Full numerical simulations of Eqs. 1 and 2 for the master and slave OMOs confirm the observation of locking (Fig. 3.4 (b), (d)). The dynamics of the slave OMO and the master OMO are simulated with experimentally-derived parameters. The set of coupled optical and mechanical equations (Eqs. 3.1, 3.2) are numerically integrated using commercially available software ([112], Appendix B). The power in the optical-drive for the slave $|s_{slave}|^2$ (Eq. 2) in the simulation contains a signal $\gamma[f(x_{master})]$, which is proportional to the transmitted signal from the master OMO. As the gain is increased, the slave is locked to the oscillations of the master OMO. The simulations also reproduce, qualitatively, major features of the dynamics, including injection-pulling [78].

This demonstration of master-slave locking of two OMOs separated by kilometers of fiber utilises a reconfigurable coupling scheme that can be easily extended to include mutual coupling between the two oscillators as well as to implementing a large network of oscillators with arbitrary network topologies. The ability to tune the coupling strength arbitrarily enables access to various regimes of nonlinear dynamics of such oscillator networks.

CHAPTER 4

SYNCHRONIZATION OF DELAY-COUPLED MICROMECHANICAL OSCILLATORS

Time-delay in coupled systems is ubiquitous in nature because of the finite propagation speed of any signal, and because of the finite response time of physical systems (e.g. neuronal networks [26, 27], chemical reactions [32], biochemical systems [97, 96, 82, 51]). Delayed-coupling can significantly influence the behaviour of coupled systems [26, 27, 32, 97, 96, 82, 23, 52, 75, 86, 105, 106, 103]. In particular, for two coupled oscillators, the presence of a time-delay could enable a multitude of stable states of synchronised oscillations [23, 52, 86, 105, 97, 96]. Recently, synchronisation of micromechanical oscillators has attracted a lot of attention [90, 112, 43, 42, 62, 25, 111, 11, 70, 3, 41] due to potential applications in communication [17], signal-processing [93], as well as in novel complex networks [43, 92]. However, effects of delayed-coupling have not yet been experimentally demonstrated on this technologically important platform.

A major challenge is to effectively introduce significant time-delay in systems of coupled micromechanical oscillators. Existing schemes [90, 112, 111, 11, 70, 3] for mutual synchronisation require the micromechanical oscillators to be in physical proximity, restricting the types of coupled-dynamics that the system can exhibit. Micromechanical oscillators can interact via electronic coupling [3, 70] or elastic coupling [90], both of which are fundamentally lossy and require the oscillators to be separated by a distance much smaller than their oscillation wavelengths, thereby rendering the time-delay insignificant.

Coupling micromechanical oscillators via light can help overcome the limitation of distance, since light can propagate with negligible loss over long distances [76]. Light-

mediated mutual synchronization of micromechanical oscillators that has been demonstrated thus far [11, 112, 111] has been with optomechanical oscillators (OMOs) that interact via a common optical microresonator, which requires them to be separated by only a few microns.

In this chapter, we synchronise two independent OMOs by mutually coupling them with an effective delay of approximately 4.5 times their oscillation time period. This scheme is based on using the radio-frequency (RF) oscillations of one oscillator to modulate the optical drive, and thereby influence the time-evolution of the phase of oscillations of the other oscillator, and vice-versa (as shown in Chapter 3). Each OMO can be modelled as a mechanical oscillator (Eq. 4.1, see Appendix C for details), with natural frequency Ω and damping rate Γ. It is driven into self-sustained, free running, oscillations by a position-dependent ($x(t)$) optical force $F_{opt}(x(t))$, provided by a continuous wave laser [55]. This force on one OMO is modulated by the mechanical displacement signal of the other OMO (and vice-versa) $x(t-T)$ after a propagation delay of T and a coupling-constant γ. Therefore, $T \approx 4.5 \times {}^{2\pi}/_{\Omega}$.

$$\ddot{x}_{i,j}(t) + \Gamma \dot{x}_{i,j}(t) + \Omega_{i,j}^2 x_{i,j}(t) = F_{opt\,i,j}(x_{i,j}(t))[1 + \gamma_{ij,ji} x_{j,i}(t-T)] \tag{4.1}$$

Each oscillator used in this experiment has a double micro-disk structure (Fig. 4.1), that supports coupled optical and mechanical resonances, and is driven into self-sustained, free running, oscillations with an external laser. The double micro-disk structure is composed of two, vertically stacked, suspended microdisks with a spacer between them (Fig. 4.1(a)). The top and bottom disks are made of low-pressure chemical vapour deposition (CVD) grown Si_3N_4, and are nominally 248 nm and 220 nm thick, respectively. The spacer is made of 170 nm thick plasma-enhanced CVD grown SiO_2. This stack rests on a 4 μm thick substrate of thermally grown SiO_2. These thin films were pat-

terned into disks with a 20 μm radius using electron-beam lithography and inductively-coupled reactive ion etching. The SiO_2 layers are partially etched away with buffered hydrofluoric acid to release the periphery of the disks (Fig. 4.1(b)). The resultant structure supports a high-quality-factor whispering gallery optical mode that is coupled to the out-of-phase mechanical resonance of the two disks (Fig. 4.1(a)). The coupling strength between the optical and mechanical degrees of freedom is characterised by the optomechanical coupling-constant $G_{\mathrm{om}} = -2\pi \times 45$ GHz/nm, as deduced from finite element simulations [112].

We optically couple two OMOs with individual mechanical oscillation frequencies of 32.9 MHz and 32.97 MHZ with a total delay of 139 ns (effective distance of 28.5 m) between them. The delay between the two oscillators is introduced using low loss optical fibres, which propagate the transmitted optical signal over a distance (Fig. 4.2). The RF oscillations of OMO 1 (Fig. 4.2) are carried by light over the optical delay line, and converted to an electrical signal at a high-speed photodetector. This electrical signal modulates the power of the laser driving OMO 2 (using an electro-optic modulator, EOM 2), thereby coupling OMO 1 to OMO 2. Similarly, OMO 2 couples to OMO 1 via EOM 1.

The strength of this coupling is controlled with a variable-gain RF amplifier (VGA 1,2), that can provide an arbitrary gain between -26 dB and +35 dB. The coupling strengths κ_{ij} (i,j = 1,2) are defined as $\kappa_{ij} = \frac{H_{inj,i}}{H_{osc,j}}$, where $H_{osc,j}$ is the oscillation power of OMO 'j', and $H_{inj,i}$ is the power of the signal from OMO 'i' imparted on the laser (via EOM 'j') driving OMO 'j'. κ_{12} is controlled by VGA 1 and κ_{21} is controlled by VGA 2. The ratio $\frac{\kappa_{12}}{\kappa_{21}}$ is kept fixed, using a third VGA (not shown in schematic in Fig. 4.2).

We show that the two oscillators transition from oscillating independently to oscillating in a synchronised manner at an intermediate frequency as we increase the coupling

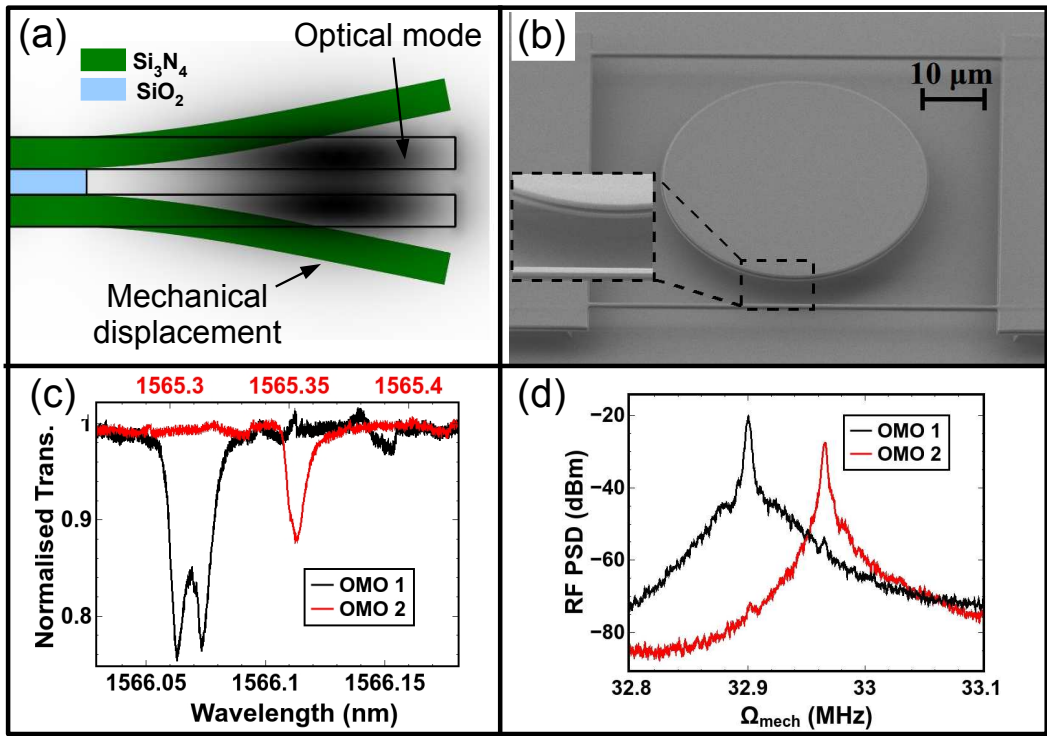

Figure 4.1: **(a)** Schematic cross-sectional picture of the periphery of a typical optomechanical (OM) resonator, indicating the co-localisation of optical and mechanical modes. **(b)** SEM image of a typical double-disk OM resonator, surrounded by a structure to support tapered optical fibers used to optically excite mechanical oscillations. **(Inset)** Higher-magnification image of the double micro-disk structure **(c)** Normalised optical transmission spectra of the two OM resonators used in this demonstration. **(d)** Power spectrum of the transmitted optical power modulated as each device is driven into self-sustained oscillations. The oscillation frequencies are separated by 70 kHz.

strength. When the oscillators are weakly coupled (small values of κ_{12}, κ_{21}), they oscillate at their individual frequencies (Fig. 4.3). As the coupling strength is increased, we observe frequency-pulling [25, 78] i.e. the frequencies of the two oscillators are pulled towards each other, while they still oscillate independently, prior to the onset of synchronised oscillations. As the coupling strength is increased beyond a threshold value, (κ_{21},κ_{12}) (-10.5 dB, -4.1 dB), (-12.13 dB, 1.5 dB) for Figs. 4.3(a) and 4.3(b) respectively, the two oscillators spontaneously begin to oscillate in synchrony, as indicated by

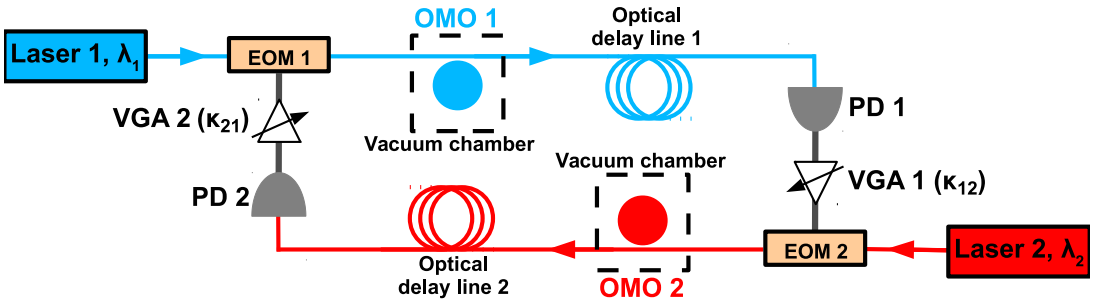

Figure 4.2: Schematic of experimental setup to synchronise two optomechanical oscillators (OMOs). Each device is driven by an independent laser tuned to be blue-side of its optical resonance. The transmitted optical signals, modulated by each OMO, travel over 9 m long delay line of SMF-28 optical fibres. The RF signal generated at the photodetector (PD) at the end of optical delay line 1 modulates the power of the laser driving OMO 2 via an electro-optic modulator (EOM), and vice-versa. The strengths of these modulation signals are controlled by variable-gain RF amplifiers (VGA). Half of the RF oscillation signal is tapped off at each of the photodetector for analysing with an RF spectrum analyser (See Appendix C for a more detailed schematic).

the emergence of a single RF tone in the transmitted optical power spectrum.

We demonstrate that these OMOs also exhibit multiple stable states in which they oscillate synchronously, as opposed to just a single stable synchronised state seen in systems without delay [23, 86, 52]. The different stable synchronised oscillations, which have different frequencies, can be accessed by selecting appropriate values for the coupling constants, κ_{21} and κ_{12}, which determine the strength with which OMO 2 couples to OMO 1, and vice versa. For instance, as shown in Fig. 4.3(a) ($\frac{\kappa_{12}}{\kappa_{21}}$ = 6.32 dB) not only do the two oscillators synchronise (κ_{21}=-10.5 dB) but also a second synchronisation frequency is seen merely by increasing κ_{21} further (κ_{21}=-6.5 dB). Similarly, for $\frac{\kappa_{12}}{\kappa_{21}}$ = 13.63 dB (Fig. 4.3(b)), we see three synchronised states beyond the synchronisation

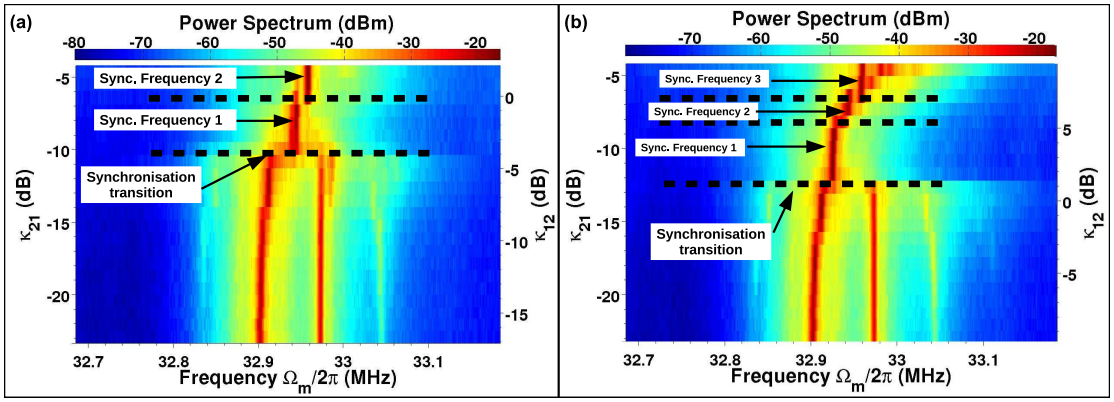

Figure 4.3: Combined power spectrum of the transmitted optical power of the two OMOs, as a function of increasing coupling strengths κ_{21} (κ_{12}), showing the synchronisation transition, while κ_{12}/κ_{21} is kept constant at **(a)** 6.32 dB and **(b)** 13.63 dB. As κ_{21} and κ_{12} are increased beyond the synchronisation threshold, we see **(a)** 2 synchronised states and **(b)** 3 synchronised states, respectively.

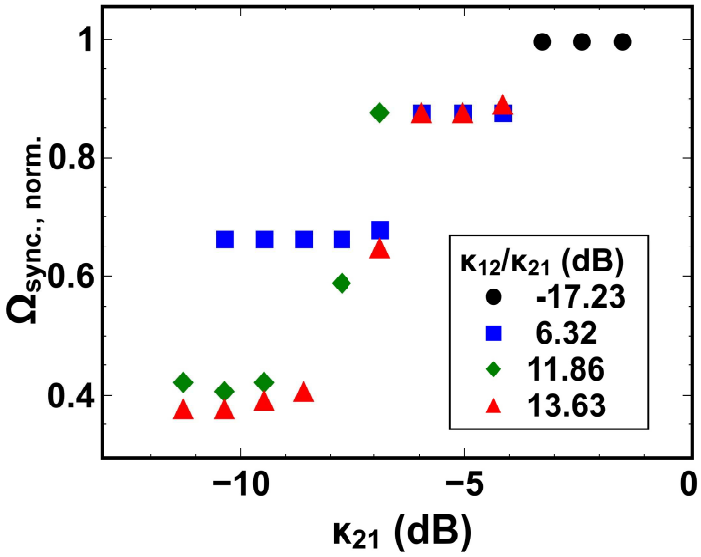

Figure 4.4: Synchronization frequency (normalised), $\Omega_{sync.,norm.}$, as obtained by varying κ_{21}, with different values of the ratio κ_{12}/κ_{21}. Blue squares (■) correspond to Fig. 4.3(a) and red triangles (▲) correspond to Fig. 4.3(b).

threshold.

$$\Omega_{sync.,norm.} = \frac{\Omega_{sync.} - \Omega_1}{\Omega_2 - \Omega_1} \tag{4.2}$$

The frequencies of the synchronised states $\Omega_{sync.}$, as a function of coupling-strength, show a clear ladder-like behaviour (Fig. 4.4), which is also found in other delay-coupled systems [86, 105]. The discrete points in Fig. 4.4 represent the frequency of the synchronised states for different values of the ratio κ_{12}/κ_{21} (as extracted from Figs. 4.3(a) and 4.3(b), and similar plots for other values of κ_{12}/κ_{21}) and plot it versus the value of κ_{21} at which they occur. Note that the gain of the VGAs, and thereby the values of κ_{21} and κ_{12} are increased in discrete steps, resulting in discrete points at each 'step' in Fig. 4.4. The value of the synchronised frequency is normalised to the frequency difference of the two oscillators as per Eq. 4.2. For a very small value of the ratio κ_{12}/κ_{21} i.e. when OMO 2 dominates the interaction between the two oscillators, the two OMOs synchronise at $\Omega_{sync.} = \Omega_2$. This is akin to master-slave locking [31], where coupling is unidirectional, from one oscillator to the other, but not vice-versa. With the ratio κ_{12}/κ_{21} set to a higher value, we observe the presence of other stable synchronised states of this system of delay-coupled OMOs. For any given ratio κ_{12}/κ_{21}, as the value of κ_{21} is increased, the two oscillators initially synchronise at a frequency close to the average of their natural oscillation frequencies. Further increase in the coupling strength gives synchronised states with frequencies that span the difference between the two natural frequencies in discrete steps.

This demonstration of controllable, multi-stable synchronisation between delay-coupled OMOs paves the way towards implementing novel memory and communication concepts [43, 17]. Delayed-coupling enables us to choose from multiple possible synchronised states, which have different oscillation frequencies enabling applications

of OMOs in distributed, reconfigurable communication networks. Delayed coupling also manifests itself in biological systems [97, 96, 51], particularly neuronal networks [26, 27, 82]. This demonstration of synchronisation of OMOs showcases a microscopic, scalable platform that could potentially be used to implement various schemes of neuromorphic information processing and computation [43, 60, 24].

CHAPTER 5

OUTLOOK : COUPLED SENSOR NETWORKS

We have shown, in this dissertation, a platform based on opto-mechanical interactions, for use in both sensing and nonlinear-dynamical applications. Therefore, it is worth considering the combination of both applications.

Individual optomechanical oscillators are potentially more sensitive than an optomechanical resonator [107, 63]. This is because, in an optomechanical resonator, the physical quantity (such as mass, displacement, etc.) being measured is transduced into a measurable change in optical power via a shift in the optical resonance, whereas in an optomechanical oscillator, the transduction takes place via a shift in the oscillation frequency peak. Optomechanical oscillators typically have a linewidth on the order of 10 Hz, limited only by thermal noise [81]. On the other hand, optical resonances have linewidths of the order of 10 MHz, which is 10^6 times larger than that of self-sustained optomechanical oscillations.

One may then conceive of two or more optomechanical oscillators, coupled as described in chapters 3 and 4, and used as sensors. Previous proposals on sensing enhanced by nonlinear interactions between coupled oscillators were based on electronic oscillators [18, 47, 48, 49]. As we described earlier, one of the limitations inherent with electronic oscillators is that the signal scatters and attenuates significantly while propagating over very short distances. As a result, those sensors have to located in close vicinity. By using optomechanical oscillators as sensors, we can, in principle, implement distributed sensor networks based on these coupled oscillators. Such networks may mimic behaviour of neuronal networks [24, 82], and potentially enable human technology with the same capabilities as the human brain.

APPENDIX A

A.1 Principle and limitations of acceleration sensing

A.1.1 Principle of operation

The canonical accelerometer consists of a displacement sensor that translates the displacement, upon acceleration, of a mass attached to a spring, into a measurable signal. When an optical cavity is used as a displacement sensor, the motion of the mass changes the optial resonance frequency. If this cavity is interrogated with a laser tuned to be at or close to the resonance, any change in the resonance frequency results in a corresponding change in laser power reflected or transmitted from the resonator. Therefore, the resulting signal directly correlates to the acceleration sensed by the test mass (Fig. A.1).

The mass-spring system can be modelled as a simple harmonic oscillator with mass m, natural frequency Ω_0, and damping Γ. The displacement $x(t)$ of the mass, under an externally applied acceleration $a_{appl}(t)$ is given by A.1.

$$\ddot{x}(t) + \Gamma\dot{x}(t) + \Omega_0^2 x(t) = a_{appl}(t) \tag{A.1}$$

Therefore, a single-tone acceleration $a(\Omega)$ induces a displacement $x(\Omega)$ according to A.2, where $\chi(\Omega)$ is the frequency-dependent mechanical susceptibility of the mass-spring system.

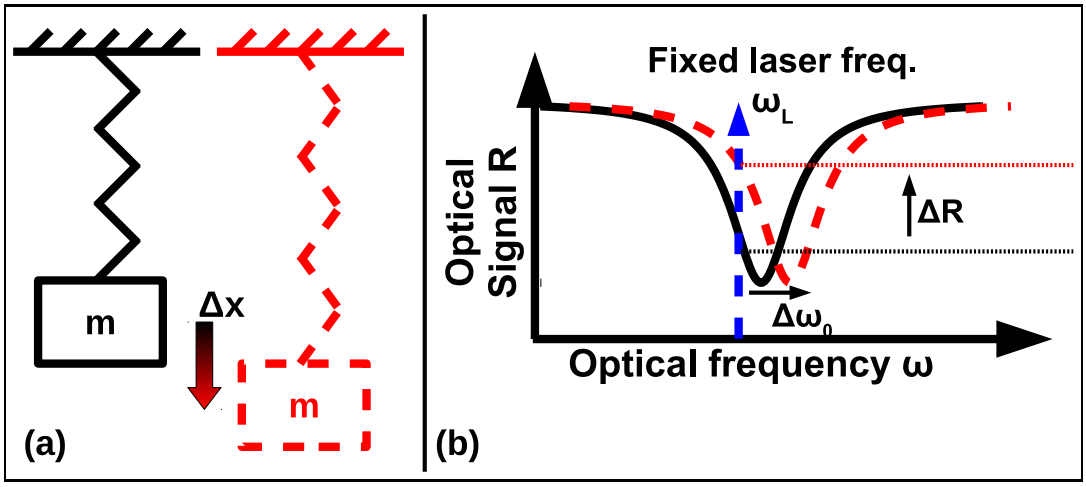

Figure A.1: **(a)** Schematic representation of a mass-spring system. A change in externally applied acceleration Δa_{appl} causes a displacement Δx of the mass. **(b)** A change in the resonance frequency $\Delta\omega_0$ of an optical cavity, results in a change in optical signal ΔR, when probed with a laser close to the resonance frequency.

$$x(\Omega) = \chi(\Omega)a(\Omega), \text{ where}$$
$$\chi(\Omega) = \frac{1}{(\Omega_0^2 - \Omega^2) + i\Gamma\Omega} \tag{A.2}$$

Accelerometers are typically operated at frequencies below the mechanical-resonance frequency Ω_0 of the mass-spring system. Therefore, Ω_0 defines the operational bandwidth of the sensor, over which the displacement produced is proportional to the acceleration applied, according to A.3.

$$x(\Omega) \approx \frac{a(\Omega)}{\Omega_0^2} \tag{A.3}$$

This implies that for accelerometers with a large Ω_0 intended for broadband operation, either with a stiffer spring or a smaller mass, the displacement resulting from a given acceleration will be smaller, thereby requiring a highly sensitive displacement sensor to accurately measure the applied acceleration.

The sensitivity of the optical resonator that is used as the displacement sensor depends on the quality factor (Q_{opt}) of the optical resonance, and the strength of optical interaction (G_{om}) between the cavity and test-mass. G_{om} ($= \frac{\Delta\omega_0}{\Delta x}$) describes the change in optical resonance frequency $\Delta\omega_0$ for a given displacement Δx of the test-mass. If R is the fractional amount of optical power output from the cavity, the sensitivity of the displacement sensor is given by A.4

$$\frac{\Delta R}{\Delta x} = \frac{\Delta R}{\Delta\omega_0}\frac{\Delta\omega_0}{\Delta x} = \frac{\Delta R}{\Delta\omega_0}G_{om} \tag{A.4}$$

Higher sensitivity is achieved by increasing either $\frac{\Delta R}{\Delta\omega_0}$ (which varies inversely as (Q_{opt})), or (G_{om}), or both.

A.1.2 Sources of noise

Thermomechanical Noise

According to fluctuation-dissipation theorem, a simple harmonic oscillator as described above, in contact contact with a thermal bath of temperature T, experiences a stochastic force F_{th}. This force has a white power spectral density proportional to the mass m and damping rate Γ, and results in an acceleration noise a_{th}, given by A.5 [83].

$$a_{th} = \sqrt{\frac{4k_B T\Gamma}{m}} \tag{A.5}$$

The contribution of this thermomechanical acceleration noise can be reduced by reducing mechanical damping Γ (i.e. by increasing mechanical quality factor Q_m) or by using a heavier test-mass m or both.

Readout Noise

According to A.4, fluctuations in displacement Δx are transduced into fluctuation in the fractional amount of optical power output from the cavity $\Delta R = \frac{\Delta P_{\text{out}}}{P_{\text{out}}}$. Conversely, any noise externally added to ΔP_{out} reduces the accuracy with which Δx, and therefore, a_{appl} can be measured.

Quantum fluctuations in the intensity of laser light (i.e. shot noise) have a white power spectral density (PSD) and contribute frequency-independent noise δP_{SN}, which for a laser frequency ω_{L}, and input power P_{in}, is given by A.6

$$\delta P_{\text{SN}} = \sqrt{2\hbar\omega P_{\text{in}}} \tag{A.6}$$

Electronic fluctuations in the photodetector also contribute a frequency-independent noise δP_{det}, equal to the noise-equivalent-power (NEP) of the photodetector. For example, a typical photodetector Newport 818-IR has an NEP of 0.6 pW/ $\sqrt{\text{Hz}}$

The noise-equivalent-displacement (NED) corresponding to these external noise sources $\delta P_{\text{SN/det}}$, can therefore be given by,

$$\delta x_{\text{SN/det}} = \frac{\delta P_{\text{SN/det}}}{P_{\text{out}} \frac{\Delta R}{\Delta\omega_0} \text{G}_{\text{om}}} \tag{A.7}$$

Therefore, according to A.7, by increasing the sensitivity of the displacement sensor ($\frac{\Delta R}{\Delta\omega_0}\text{G}_{\text{om}}$) we can reduce the influence of these external noise contributions.

A.2 Fabrication of devices

The fabrication process is schematically depicted in Fig. A.2

We fabricate optical and mechanical components on separate Si wafers using SiN grown using low-presure (LP) chemical vapour deposition (CVD). The optical components are patterned in SiN, grown using LPCVD on thermal SiO, using e-beam lithography and reactive ion etching (RIE) in an inductively coupled plasma (ICP). The devices were clad with SiO that was deposited using plasma enhanced (PE) CVD. Windows were patterned and, then etched using buffered HF, around the rings to allow the membrane to get close to the optical mode in the ring.

The membrane and nanotethers are patterned together using photolithography and ICP-RIE on 200 nm thick SiN. The SiN film is deposited using LPCVD on a substrate of 2.1 μm thick plasma-enhanced (PE) CVD SiO deposited on an Si wafer. The membrane and tethers are clad with 2.1 μm thick PECVD SiO for subsequent processing. The proof mass is defined on a similar SiO/SiN/SiO stack on the backside of the same wafer, and is released from the surrounding substrate using a combination of anisotropic Deep-RIE (DRIE) and isotropic chemical vapour etching using XeF_2. Additional tethers are patterned on the back side while defining the proof mass in order to provide mechanical stability to the whole assembly. The SiO cladding around the SiN tethers is then etched away using HF vapour.

A.3 Mechanical frequencies

Each nanotether of length L, width W and thickness t can be modelled as two back-to-back, end-loaded cantilevers of length $L/2$. The mechanical resonance frequency of N

such nanotethers, supporting a mass *m* can be given by A.8 [67], where E is the Young's modulus of SiN.

$$\Omega_0 = \sqrt{\frac{N(E/2)Wt^3}{4m(L/2)^3}} \tag{A.8}$$

Figure A.2: Fabrication process flow

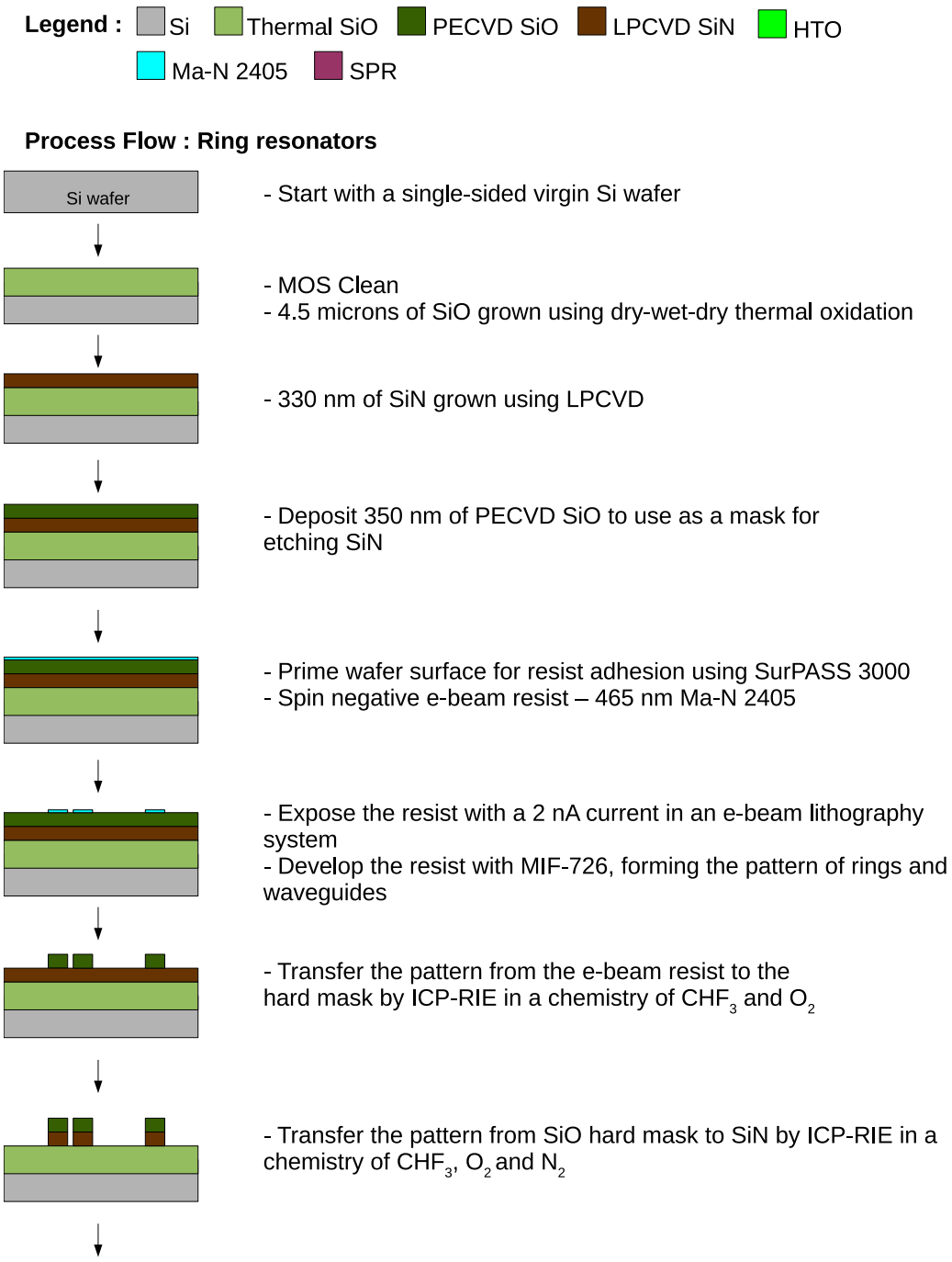

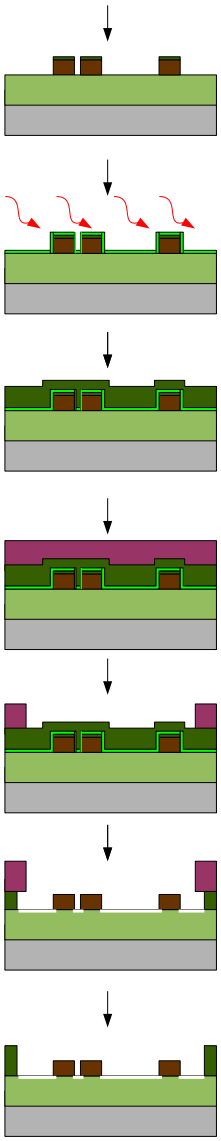

- Strip residual resist using Microposit Remover 1165
- Partially etch remaining hard mask using ICP-RIE.

- MOS clean
- Furnace anneal at 1200^{0}C for 3 hours
- Deposit 200nm of HTO as optical cladding

- Deposit 850nm PECVD SiO as optical cladding

- Dehydrate wafer and prime the surface with HMDS for resist adhesion
- Spin positive photoresist SPR 220-3.0, ~2.6 microns
- Bake at 115^{0}C, 3 minutes

- Expose the photoresist using photolithography
- Post-exposure bake – 115^{0}C, 3 mins
- Develop the resist in MIF-726, to open windows around the ring-resonators

- Etch windows into the SiO cladding (HTO + PECVD) using 6:1 buffered HF solution

- Strip away the remaining photoresist with a long soak using heated AZ300T resist stripper

Process Flow : Etching input-output coupling facets

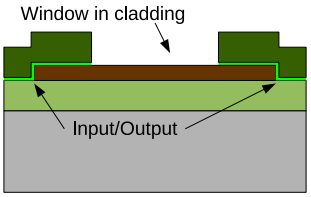

Side cross sectional view of the waveguide, showing the waveguide input and output and the window opened in the cladding around the ring resonator.

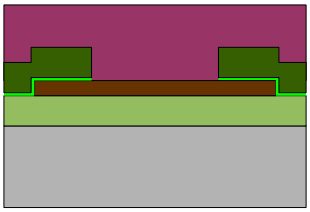

- Dehydrate wafer and prime the surface with HMDS for resist adhesion
- Spin positive photoresist SPR 220-7.0, ~7.5 microns
- Bake at 90^{0}C for 30secs, 115^{0}C for 3 minutes, 90^{0}C for 30secs

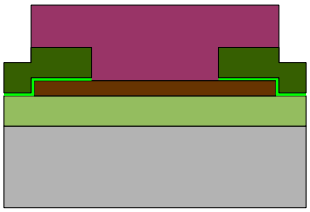

- Expose the photoresist using photolithography
- Let photoresist rest in order to rehydrate – 2 hours
- Post-exposure bake – 90^{0}C for 30secs, 115^{0}C for 3 minutes, 90^{0}C for 30secs
- Develop the resist in MIF-726, to define edges of coupling facets

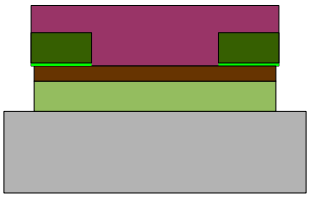

- Etch the SiO layers using ICP-RIE, in a CHF_3+O_2 chemistry, all the way down to the Si substrate

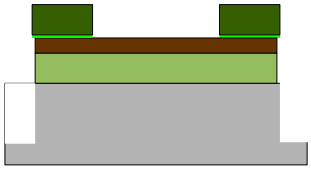

- Etch about 150 microns down into the Si substrate using Bosch DRIE etch
- Strip away the remaining photoresist with a long soak using heated AZ300T resist stripper

Process Flow : Fabricating SiN membranes supporting a large proof mass, suspended by High-Q SiN tethers

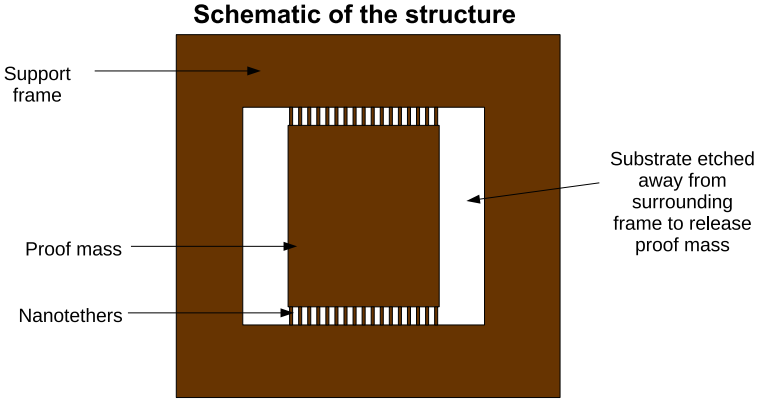

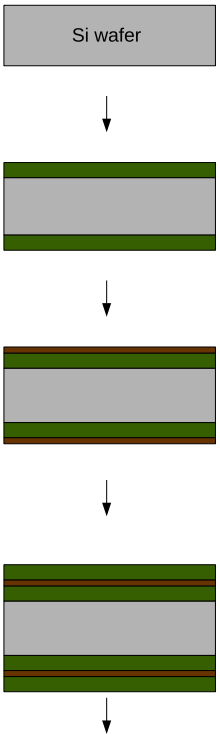

- Start with a double-sided virgin Si wafer

- Deposit 2.1 microns of PECVD SiO on both sides of the wafer

- MOS clean
- Deposit SiN using LPCVD. The thickness depends on the design of tethers. Typically, 200 nm thick.

- Deposit 2.1 microns of PECVD SiO on both sides of the wafer

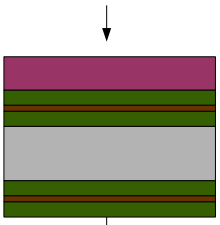

- Dehydrate wafer and prime the surface with HMDS for resist adhesion
- Spin positive photoresist SPR 220-7.0, ~7.5 microns on front side of the wafer
- Bake at 90^0C for 30secs, 115^0C for 3 minutes, 90^0C for 30secs

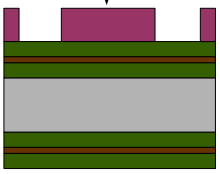

- Expose the photoresist using photolithography
- Let photoresist rest in order to rehydrate – 2 hours
- Post-exposure bake – 90^0C for 30secs, 115^0C for 3 minutes, 90^0C for 30secs
- Develop the resist in MIF-726, to define the membrane and tethers

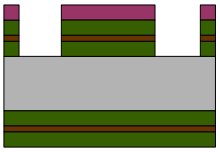

- Etch through the SiO and SiN layers, all the way down to the Si substrate using ICP-RIE, in a CHF_3+O_2 chemistry

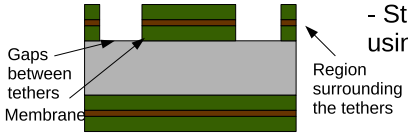

- Strip away the remaining photoresist with a long soak using heated AZ300T resist stripper

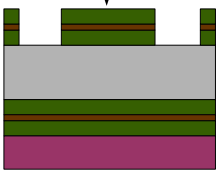

- Dehydrate wafer and prime the surface with HMDS for resist adhesion
- Spin positive photoresist SPR 220-7.0, ~7.5 microns on back side of the wafer
- Bake at 90^0C for 30secs, 115^0C for 3 minutes, 90^0C for 30secs

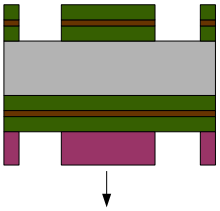

- Expose the photoresist using photolithography
- Let photoresist rest in order to rehydrate – 2 hours
- Post-exposure bake – 90^0C for 30secs, 115^0C for 3 minutes, 90^0C for 30secs
- Develop the resist in MIF-726, to define the proof mass and support tethers on the back, aligned to the membrane on the front side

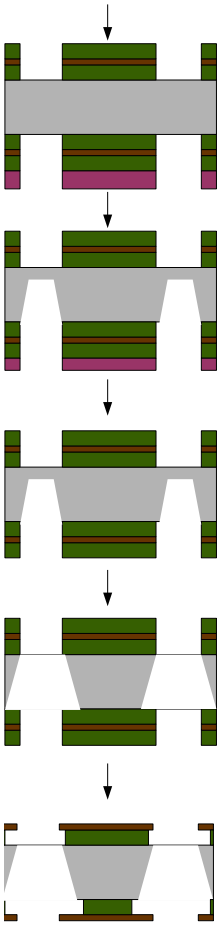

- Etch through the SiO and SiN layers, all the way down to the Si substrate using ICP-RIE, in a CHF_3+O_2 chemistry

- Pattern the proof mass from the surrounding Si substrate by etching almost entirely through the wafer (from the back side) using Bosch DRIE etch.
  Note the portion of the Si substrate masked by the support tethers on the back side remains unetched

- Strip away the remaining photoresist with a long soak using heated AZ300T resist stripper

- Etch away the Si that was left unetched during the previous DRIE step using XeF_2 vapour. This step fully releases the proof mass from the surroundign Si substrate

- Etch away the SiO cladding SiN tethers (on both sides of the tethers, both on the front and the back of the wafer), using HF vapour.
- This also etches away the SiO cladding the membrane, so that the SiN membrane can perturb the ring resonator

APPENDIX B

B.1 The Optomechanical oscillator

An optomechanical oscillator can be described by a set of coupled equations describing the optical mode (Eq. B.1) and the mechanical mode (Eq. B.2). Chapter 3 provides a physical description of these equations.

$$\frac{da}{dt} = i(\Delta_0 - G_{\mathrm{om}}x)a - \Gamma_{opt}a + \sqrt{2\Gamma_{ex}}s \tag{B.1}$$

$$\frac{d^2x}{dt^2} + \Gamma_m\frac{dx}{dt} + \Omega_m^2 x = \frac{F_{opt}[a]}{m_{eff}} \tag{B.2}$$

In the 'bad cavity limit', i.e. in the case where the optical decay rate Γ_{opt} is much larger than the mechanical frequency ($\Gamma_{opt} \gg \Omega_m$), for a given displacement x, the optical cavity reaches a steady state much faster than the mechanical resonator responds to the change in $F_{opt}[a]\left(= \frac{G_{\mathrm{om}}|a|^2}{\omega}\right)$. Therefore, in this limit, one may analyse Eq. B.1 quasistatically, with a value of x delayed by the response-time $\tau(= \frac{1}{\Gamma_{opt}})$ of the optical cavity. This delay accounts for the fact that although the optical cavity responds much faster than the mechanical resonator, it does not do so instantaneously. Therefore, the steady state value for a is given by Eq. B.3, and substituting it in Eq. B.2 yields an equation for mechanical motion (Eq. B.2) in the quasistatic approximation for the optical cavity.

$$a(t) = \frac{\sqrt{2\Gamma_{ex}}s}{i(\Delta_0 - G_{\mathrm{om}}x(t-\tau)) - \Gamma_{opt}} \tag{B.3}$$

$$\frac{d^2x(t)}{dt^2} + \Gamma_m\frac{dx(t)}{dt} + \Omega_m^2 x(t) = \frac{g_{om}}{m_{eff}\omega}\frac{2|s|^2\Gamma_{ex}}{(\Delta_0 - G_{\mathrm{om}}x(t-\tau))^2 + \Gamma_{opt}^2} \tag{B.4}$$

Eq. B.4 can be simplified by normalising the displacement ($y = \frac{G_{\mathrm{om}}x}{\Delta_0}$) and time ($T = t\Omega_m$), and substituting $A = \frac{2G_{\mathrm{om}}^2\Gamma_{ex}}{m_{eff}\omega\Omega_m^2\Delta_0^3}$, $B = (\frac{\Gamma_{opt}}{\Delta_0})^2$, and $Q_m = \frac{\Omega_m}{\Gamma_m}$, to give

$$\frac{d^2y(T)}{dT^2} + \frac{1}{Q_m}\frac{dy(T)}{dT} + y = \frac{A|s|^2}{B + (1 + y(T - \tau\Omega_m))^2} \tag{B.5}$$

B.2 Oscillation power and Injection Ratio

When an optomechanical cavity is excited with a laser of power $|s|^2$ via a waveguide coupled to the optical cavity with a coupling constant $\sqrt{2\Gamma_{ex}}$, the power exiting the cavity is given by $|s_{out}|^2 = |s - \sqrt{2\Gamma_{ex}}a|^2$ [39]. Using Eq. B.3, and letting D_g represent the transimpedance gain of the detector and input gain of the spectrum analyzer, the power detected at the spectrum analyzer can be written as

$$P_{trans}(x) = D_g|s|^2|1 - \frac{2\Gamma_{ex}}{i(\Delta_0 - G_{\mathrm{om}}x) - \Gamma_{opt}}|^2 \tag{B.6}$$

If x oscillates at the frequency Ω_{osc} i.e. $x = x_0\cos(\Omega_{osc}t)$, P_{trans} can be approximated in terms of its spectral components, i.e. as a Fourier series Eq. S5, where $D_g|s|^2(P_0, P_1, P_2, ...)$ are the power-spectral-density (PSD) values of P_{trans} at the frequencies $(0, \Omega_{osc}, 2\Omega_{osc}, ...)$. This approximation holds because the linewidth reduces dramatically when oscillations begin [55], and most of the power in the spectral component is concentrated at the centre-frequency itself. Harmonics are introduced because of the non-linear transduction between x and P_{trans}. It must be noted that $(P_0, P_1, P_2, ...)$ are functions of x_0 since they are Fourier coefficients of $|1 - \frac{2\Gamma_{ex}}{i(\Delta_0 - G_{\mathrm{om}}x) - \Gamma_{opt}}|^2$

$$P_{trans} = D_g|s|^2 \left(P_0 + P_1 \cos(\Omega_{osc}t) + P_2 \cos(2\Omega_{osc}t) + ...\right) \tag{B.7}$$

The parameter H_{slave} from the Chapter 3 can, therefore, be written as $H_{slave} = D_{g,slave}|s_{slave}|^2 P_{1,slave}$. This value is directly read off the spectrum analyzer.

The output of the master oscillator modulates the laser driving the slave, as per Eq. 3.3 in the Chapter 3 (Also see section 'Electro-optic coupling'). The modulation function $f(x_{master})$ is proportional to Eq. B.7, where all the PSD values correspond to the master oscillator. Assuming that the harmonics are negligible compared to the fundamental frequency component i.e. coefficient of $\cos(\Omega_{inj}t)$, Eq. 3.3 from the Chapter 3 can be rewritten as Eq. B.8, where the detector transimpedance gain $D_{g,master}$, propagation loss, modulation gain from the electro-optic modulator and the variable RF amplifier gain, are absorbed into the variable parameter γ.

$$|s_{slave}|^2 = |s_{0,slave}|^2(1 + \gamma \cos(\Omega_{inj}t)) \tag{B.8}$$

$$\begin{aligned} P_{trans,slave} =& D_{g,slave}|s_{0,slave}|^2(1 + \gamma \cos(\Omega_{inj}t)) \\ & (P_{0,slave} + P_{1,slave} \cos(\Omega_{osc}t) + P_{2,slave} \cos(2\Omega_{osc}t) + ...) \end{aligned} \tag{B.9}$$

Substituting Eq. B.8 in Eq. B.7 gives Eq. B.9, from which we can find the PSD of $P_{trans,slave}$ at the frequency Ω_{inj}. The parameter H_{inj} from the Chapter 3 can, therefore, be written as $H_{inj} = D_{g,slave}|s_{slave}|^2 P_{0,slave}\gamma$. This value, too, is directly read off the spectrum analyzer.

Therefore, the injection ratio $\dfrac{H_{inj}}{H_{slave}}$ equals the ratio of the relative amplitudes of modulations of the optical power in the waveguide (i.e. ratio of modulation depths), caused by injected signal and the free-running slave oscillator, i.e.

$$\frac{H_{inj}}{H_{slave}} = \frac{\gamma}{P_1/P_0} \tag{B.10}$$

Electro-optic coupling

We use an electro-optic modulator to couple master oscillator to the slave oscillator. The RF power transmitted from the master oscillator ($P_{trans,master}$) modulates the optical power transmitted through the modulator as per Eq. B.11 [16], where Γ accounts for the gain of the amplifier (see Chapter 3) and the modulator.

$$|s|^2 = |s_0|^2(1 + \frac{1}{2}\sin(\Gamma P_{trans,master})) \tag{B.11}$$

$$|s|^2 = |s_0|^2(1 + \frac{\Gamma}{2}P_{trans,master}) \tag{B.12}$$

For sufficiently small values of $\Gamma P_{trans,master}$, Eq. B.11 can be written as Eq. B.12. For a sinusoidal variation of $P_{trans,master}$ (Eq. B.8), the modulation term on the RHS of Eq. B.11 can be expanded in terms odd harmonics of Ω_{inj} [1]. Therefore, the smallest harmonic corresponds to $3\Omega_{inj}$, and the component corresponding to $2\Omega_{inj}$ is absent.

B.3 Frequency-locking of optomechanical oscillators

Optomechanical back-action [55], which amplifies or dampens mechanical oscillations, occurs because the optical-force has a component in phase with the velocity of the mechanical resonator. This is because the optical cavity does not respond instantaneously (i.e. $\tau \neq 0$). However, this also makes analysing Eq. B.5 and frequency-locking difficult, because it is a delay-differential equation.

The oscillation amplitude and phase (frequency) of optomechanical oscillators are not mutually independent, as demonstrated by the optomechanical spring effect [55]. As a result, the well-known Adler equation [2, 78] which models injection-locking of oscillators via phase-only coupling, does not adequately reflect the dynamics of locking of optomechanical oscillators represented by Eq. B.5.

In this section, we will reduce Eq. B.5, under appropriate approximations, to a variant of the well-known Mathieu equation [77], which will serve as a template to understand locking behaviour in optomechanical oscillators.

B.3.1 Simplfied Model Based on Mathieu Equation

The optomechanical oscillator begins undergoing self-sustained oscillations (limit-cycle oscillations) as the laser power crosses a threshold value which is determined by $\frac{1}{Q_m}, A, B$ and τ [55]. Below this threshold laser power, oscillation-amplitude decays due to mechanical damping. If we neglect damping, i.e. $\frac{1}{Q_m} = 0$, we can assume $\tau = 0$ and still have oscillatory solutions to the equation, with a sustained oscillation-amplitude. This gives us

$$\frac{d^2y}{dT^2} + y = \frac{A|s|^2}{B + (1 + y)^2} \tag{B.13}$$

When damping is neglected, even small values of y (i.e. the change in optical resonance frequency caused by mechanical motion is much smaller than the linewidth of the optical resonance) correspond to oscillatory motion. Therefore, Eq. B.13 can be further simplified by assuming $y \ll 1$, and considering only the first three terms from the Taylor expansion of the RHS around $y = 0$, giving Eq. B.14. We include the lowest-order

nonlinear term (i.e. the quadratic term) to analyse the effect of nonlinearity in locking, and include amplitude-frequency coupling in the analysis.

$$\frac{d^2y}{dT^2} + y = \frac{A|s|^2}{(1+B)^3}((1+B)^2 - 2(1+B)y - (B-3)y^2) \tag{B.14}$$

The laser power $|s|^2$ is modulated by an external signal from the master oscillator, as per Eq. B.8. Substituting this in Eq. B.14, and rearranging terms gives Eq. B.15, where $E_1 = 2\frac{A|s_0|^2}{(1+B)^2}, E_2 = \frac{(B-3)E_1}{2(1+B)}, E_0 = (1+B)\frac{E_1}{2}, \Omega = \frac{\Omega_{inj}}{\Omega_m}$.

$$\frac{d^2y}{dT^2} + (1 + E_1 + \gamma E_1 \cos(\Omega T))y + \gamma \cos(\Omega T)E_2 y^2 = E_0(1 + \gamma \cos(\Omega T)) \tag{B.15}$$

Eq. B.15 represents a forced oscillator, with parametric as well as non-parametric forcing. Note that we neglect the unforced quadratic term E_2y^2 on the LHS while deriving Eq. B.15 because, in practice, $E_2 \ll 1$, and the unforced motion is essentially simple harmonic. Non-parametric forcing of a linear oscillator gives a response at the forcing frequency, along with the natural frequency. The solution is altered only when the detuning i.e. difference between natural frequency and forcing frequency is zero. However, this case is not of interest, since we are looking for the response of the oscillator when the detuning is not zero.

Parametric forcing can lead to instability due to the parametric-resonance phenomenon [77]. These unstable oscillations are at the same frequency as the forcing frequency [77] i.e. the instability corresponds to locked oscillations. As the oscillation amplitude increases, higher-order terms, which were neglected in Eq. B.14 become significant, and limit the oscillation amplitude. However, in order to study locking, it is sufficient to study Eq. B.15 without the non-parametric forcing. Eq. B.16 is similar to

Mathieu's equation [77], and can be analysed using perturbation theory, with γ as the perturbation parameter, $U = \Omega T, \delta = \delta_0 + \gamma\delta_1 + \gamma^2\delta_2, \delta_0 = \frac{1+E_1}{\Omega^2}, D_1 = \frac{E_1}{\Omega^2}, D_2 = \frac{E_2}{\Omega^2}, y = y_0 + \gamma y_1 + \gamma^2 y_2$

$$\frac{d^2y}{dU^2} + (\delta + \gamma D_1 \cos(U))y + \gamma \cos(\Omega T) D_2 y^2 = 0 \tag{B.16}$$

We use the method of multiple time scales [77] to analyse Eq. B.16, with $\xi = U, \eta = \gamma U, \nu = \gamma^2 U$, around the parametric resonance occuring at $\delta_0 = 1$ (i.e. when forcing frequency is close to the frequency of the oscillator). Note that this case is different from the stardard analysis of parametric excitation when the excitation frequency is close to twice the oscillator frequency. Also see the section 'Electro-optic coupling'.

For a given value of normalised detuning $\Delta(= 1 - \sqrt{\delta})$ between the oscillator frequency and the forcing frequency, the perturbation parameter γ is obtained from Eq. B.17.

$$\gamma^2\delta_2 + \gamma\delta_1 + 1 - (1 - \Delta)^2 = 0 \tag{B.17}$$

Upon performing the perturbation analysis and finding conditions for the solution to be stable in each order of perturbation, we get expressions for δ_1 and δ_2 (Eqs. B.18, B.19), which represent the curves along the boundary of regions of locked and unlocked oscillations i.e. the Arnold tongue (R is the unperturbed oscillation amplitude of Eq. B.16).

$$\delta_1 = -\frac{3}{4}D_2R, \delta_2 = \frac{5}{6}D_1(\frac{D_1}{2} + D_2R) \tag{B.18}$$

$$\delta_1 = \frac{3}{4}D_2R, \delta_2 = \frac{5}{6}D_1(\frac{D_1}{2} - D_2R) \tag{B.19}$$

Substituting Eqs. B.18, B.19 in Eq. B.17 and solving Eq. B.17 for γ, we get the minimum value of γ necessary to lock the slave oscillator with a detuning of Δ.

B.3.2 Arnold tongue for frequency locking

The injection ratio $\frac{H_{inj}}{H_{slave}}$ is given by Eq. B.10, where P_0 and P_1 are the Fourier components of $|1-\frac{2\Gamma_{ex}}{i(\Delta_0 - G_{\mathrm{om}}x) - \Gamma_{opt}}|^2$ at the frequencies 0 and Ω_{inj}. Taking $x = x_0\cos(\Omega_{osc}t)$, we find from the Taylor expansion of $|1 - \frac{2\Gamma_{ex}}{i(\Delta_0 - G_{\mathrm{om}}x) - \Gamma_{opt}}|^2$ around $x = 0$,

$$\frac{P_1}{P_0} \approx \frac{8\Delta_0 G_{\mathrm{om}}\Gamma_{ex}(\Gamma_{opt} + \Gamma_{ex})x_0}{(\Gamma_{opt}^2 + \Delta_0^2)((\Gamma_{opt} + 2\Gamma_{ex})^2 + \Delta_0^2)} \tag{B.20}$$

Substituting experimental and simulated [112] values in Eqs. B.17, B.18, B.19 and B.20, and $x_0 = 10^{-11}$m [1], we get Fig. B.1, representing the Arnold tongue (as a function of modulation depth γ and normalised detuning Δ) for the locking of slave oscillator to the master oscillator. The red and blue lines on the figure indicate the detuning of the oscillators used in the experiment.

B.3.3 Comparison with experiment

It is remarkable that despite the extreme simplicity of the model used, it shows the expected trend for the minimum injection ratio required to lock as detuning increases. The values of injection ratios for locking obtained from the model, for the frequency detuning of oscillators in the experiment, are withing 5 dB of experimental values. The

[1] $G_{\mathrm{om}} = -2\pi 4.9\times10^{19}$ GHz/nm, $\Gamma_{ex} = 5.138\times10^{8}$ /s, $m_{eff} = 10^{-13}$ kg, $\omega = 1.2037\times10^{15}$ rad/s, $\Omega_m =$ 32.82 MHz, $\Delta_0 = 4.856\times10^{9}$ /s, $\Gamma_{opt} = 2.299\times10^{9}$ /s, $s_0 = 10^{-4}$ W

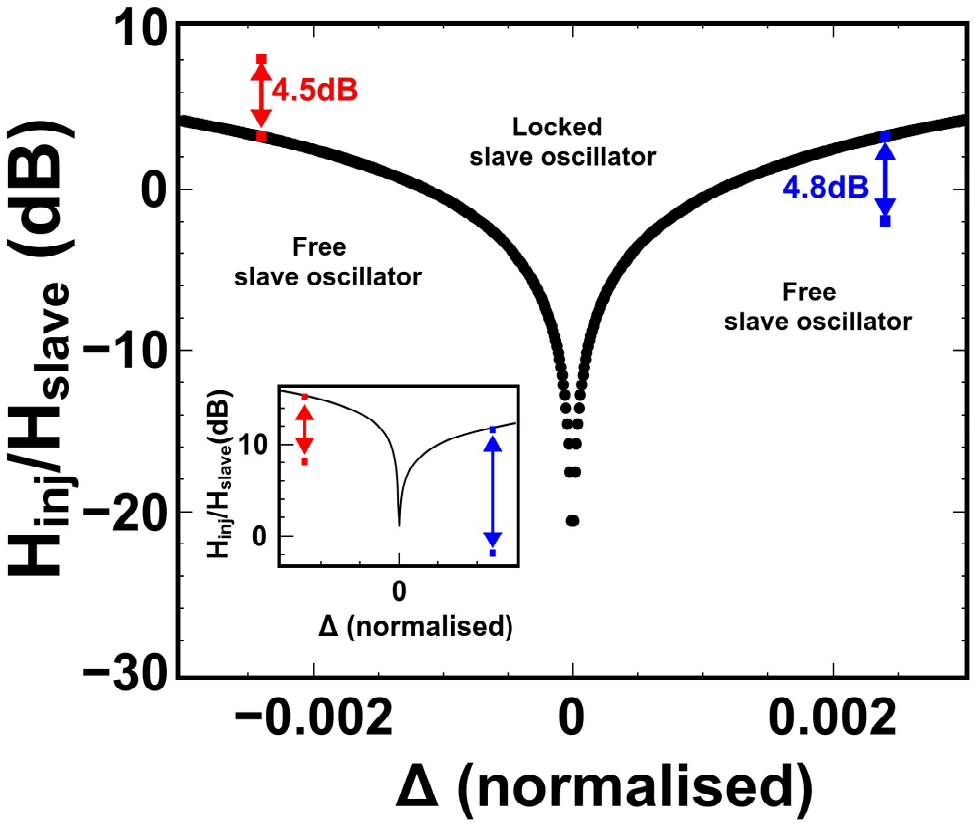

Figure B.1: Plot of the Arnold tongue i.e. the minimum value of $\frac{H_{inj}}{H_{slave}}$ required for locking, as a function of normalised detuning Δ $(= 1 - \frac{\Omega_{slave}}{\Omega_{inj}})$, obtained from Eqs. B.10, B.17, B.18, B.19 and B.20. The red and blue points **on the curve** indicate locking thresholds obtained from the analysis for the detuning of the oscillators in the Chapter 3. The arrows show that that the errors between experimental and analytical values for locking thresholds are less than 5 dB. The analysis does not hold at $\Delta = 0$, and that point is not included in the plot. Inset shows the tongue obtained by neglecting all quadratic terms.

role played by the nonlinear term is obvious from the inset of Fig. B.1, which shows the Arnold tongue obtained by performing perturbation analysis on Eq. B.16 with $D_2 = 0$. Without the nonlinear term coupling the amplitude and frequency, the minimum injection ratios obtained from the analysis are 10 dB and 14 dB larger than experimental values.

It must be emphasised that Eq. B.16 is suitable only to understand the essential features of the locking process i.e. the Arnold tongue and the role played by nonlinearities. A better match between analytical and experimental results may be obtained by considering more terms in the expansion in Eq. B.14. Specifically, the difference in the locking strength required upon switching the roles of the master and slave oscillators, as seen in the experiment, may be obtained in this model by considering higher nonlinear terms, which are known to induce an asymmetrical response [108, 73]. One may go a step further and even attempt to analyse Eq. B.5 as a delay-differntial equation. However, the analysis is significantly more challenging and beyond the scope of this work.

B.4 Numerical simulations for locking

Figs. 3.3(b) and 3.3(d), which show simulated results for master-slave locking of the two OMOs, are obtained by numerical integration of Eqs. B.1, B.2 for each OMO. We perform the calculation using the solver *NDSolve* available in the commercial software Mathematica®.

Eqs. B.1, B.2 are first solved for the master oscillator. Starting with initial values of $a_{master}(0) = 0, x_{master}(0) = 5 \times 10^{-12} m, \frac{dx_{master}}{dt} = 0$, the equations are integrated from $t_0 = 0$ to $t_{max} = 0.5$ ms. We observe from the time trace of the solution that it takes about 0.1 ms to reach steady-state oscillations. The time-dependent optical power transmitted

from the master oscillator is stored in memory for later use.

$$P_{trans,master}(t) \propto |s_{0,master} - \sqrt{2\Gamma_{ex}} a_{master}(t)|^2 \tag{B.21}$$

In the same way as for the master oscillator, Eqs. B.1, B.2 are solved for the slave oscillator, at first without any coupling between the master and the slave. We observe that just like the master oscillator, the slave also takes about 100 μs to reach steady-state oscillations. During the experiment, both the oscillators attain steady state oscillations before they are coupled together. To reflect this, the $s_{0,slave}$ is kept constant for 100 μs, before being modulated by $P_{trans,master}(t)$ (calculated earlier), as per Eq. B.22. This is accomplished by using a Heaviside Step Function, with the argument $t_c = 100$ μs, to couple the AC part of $P_{trans,master}(t)$ (Eq. B.21) to s_{slave}. The DC part is filtered out so that only the RF oscillations, not the DC value of $P_{trans,master}(t)$, couple to s_{slave}, as in the experiment.

$$|s_{slave}(t)|^2 = |s_{0,slave}|^2[1 + \mathcal{H}(t_c = 10^{-4}s) \cdot \frac{\Gamma}{2} \cdot (P_{trans,master}(t) - < P_{trans,master}(t) >)] \tag{B.22}$$

Finally, Figs. 3.3(b) and 3.3(d) are obtained by calculating and plotting the PSD of $P_{trans,slave}(t)$ for increasing values of modulation strength Γ.

Note : Although it is not essential to let the oscillators reach steady state oscillations in simulations before coupling them, doing so gives results that match better with experiments. This is because optomechanical oscillators are highly nonlinear systems, and the limit-cycle in which they oscillate is dependent on initial conditions [69]. By ensuring that the oscillations reach steady state before coupling is switched on, the numerical calculations emulate experimental initial conditions better.

B.4.1 Time-dynamics of locking

When the modulation depth γ crosses the minimum value required to lock the slave oscillator to the master oscillator, the slave oscillator undergoes a change in its dynamics. This change, however, is not instantaneous. There is a period of transient behaviour before the frequency and amplitude of the slave oscillator settle at their new steady state values.

We can obtain a rough estimate of the duration of this transient behaviour from numerical simulation of Eqs. B.1 and B.2. First, we simulate oscillations of the master oscillator, and store the time-trace of $P_{trans,master}$ (Eq. B.21). Then, we simulate for the slave oscillator, with $|s_{slave}|^2$ given by Eq. B.22. In order to observe the locking-transients, the coupling between the master and the slave oscillators is 'switched-on' at $t = t_c$, using a Heaviside step-function $\mathcal{H}(t_c = 200\,\mu\text{s})$. Note that although the individual oscillators reach steady-state oscillations after 100 μs, we simulate for an additional 100 μs before coupling the slave oscillator to the master. This enables us to analyse the steady-state oscillations of the slave oscillator both before and after coupling to the master oscillator (see next paragraph).

Fig. B.2 shows the time trace of $P_{trans,slave}$. It can be seen that the dynamics change almost instantly when coupling is switched on at $t = t_c = 200\ \mu s$. However, there are transients that persist, apparently until $t = 230\ \mu s$. This is better revealed in the Short-Time-Fourier-Transform (STFT) of the time trace in Fig. B.2(b). The STFT gives the frequency spectrum of the signal within a specified window of time. In order to obtain Fig. B.2(b) from Fig. B.2(a), we calculate the frequency spectrum (Fig. B.2(b), y-axis) using the FFT algorithm in discrete time-windows (Fig. B.2(b), x-axis) that are 10 μs long, with a 5 μs overlap between adjacent windows. We see that the dominant frequency in the spectrum is 32.91 MHz for $t \leq 200\ \mu s$, and it is 32.99 MHz for $t \geq 230$

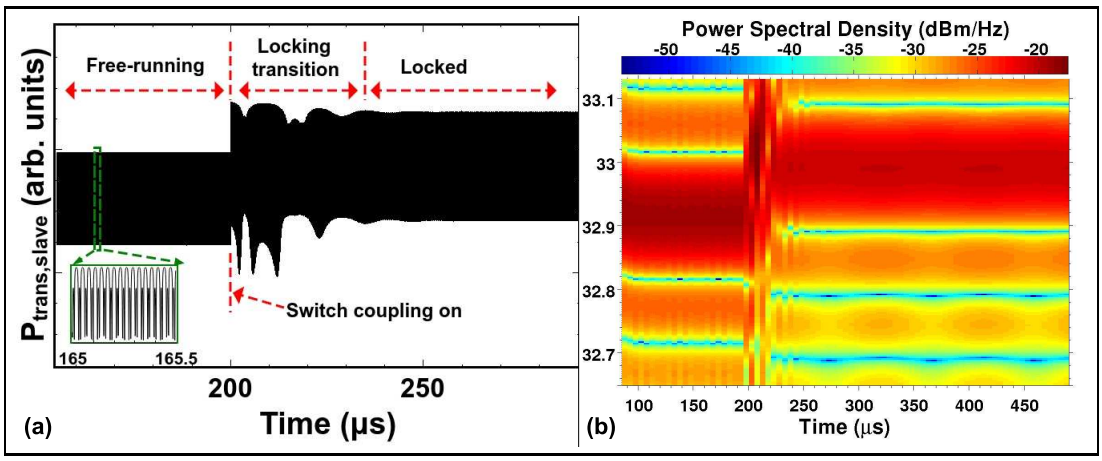

Figure B.2: (a) Simulated time-trace of $P_{trans,slave}$. Inset shows a sample of the time-trace, showing the oscillating signal, over a few cycles. (b) The STFT of the signal from part (a), using 10 μs long windows, and a time-step of 5μs. The frequency resolution of the STFT is limited by the length of the window chosen for the STFT. A longer window would give better frequency resolution, at the expense of worse time-resolution.

μs. However, for 200 $\mu s \leq t \leq$ 230 μs, it can be seen that there is a transition between the two dominant frequencies.

B.5 Phase noise of the locked oscillator

Previous studies [58, 22, 21] have shown that the close-to-carrier phase noise of the locked slave oscillator is identical to that of the master oscillator. For a freely running oscillator, the phase noise is determined by the thermal noise affecting the oscillator [81]. The spring constant of the resonator corresponds to a restoring force against perturbations to the amplitude, but there is no analogous restoring force for the phase i.e. phase perturbations add up [74]. When an external periodic force is introduced, it acts as a restoring force against phase perturbations, and serves to lock the phase of the slave to that of the master. This also results in the phase noise of the slave being identical to

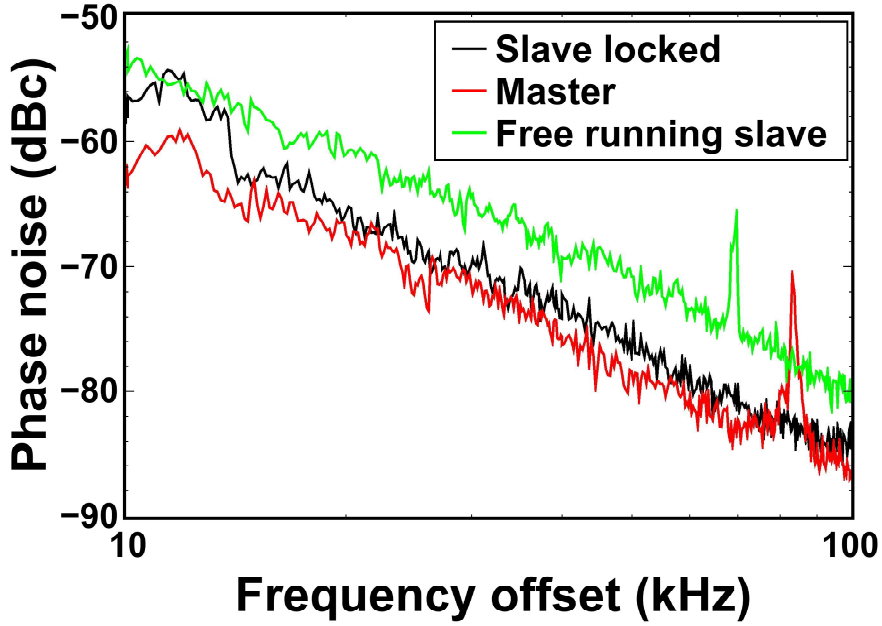

Figure B.3: Phase noise of the master oscillator, and the slave oscillator (both freely running and locked). The spurious narrow peaks seen at 70 kHz and 84 kHz can be attributed to resonances of the tapered optical fibers used to excite the master and slave oscillators.

that of the master.

Fig. B.3 shows the measured phase noise of master oscillator, and that of the slave oscillator before and after locking. It can be seen that the phase noise of the master oscillator is lower than that of the freely running slave oscillator. Upon locking, the phase noise of the slave reduces to a value close to, but slightly more than, that of the master. This difference can be attributed to the noise added by the photodetector, variable gain RF amplifier, and other electric circuitry in the path. It must be noted that this extra noise is small (e.g. 1.3 dB at 50 kHz offset). This implies that the use of a detector, RF amplifier and modulator in our scheme does not add a lot of noise and does not significantly raise the locking threshold (since noise influences the minimum injection ratio required for locking [74]).

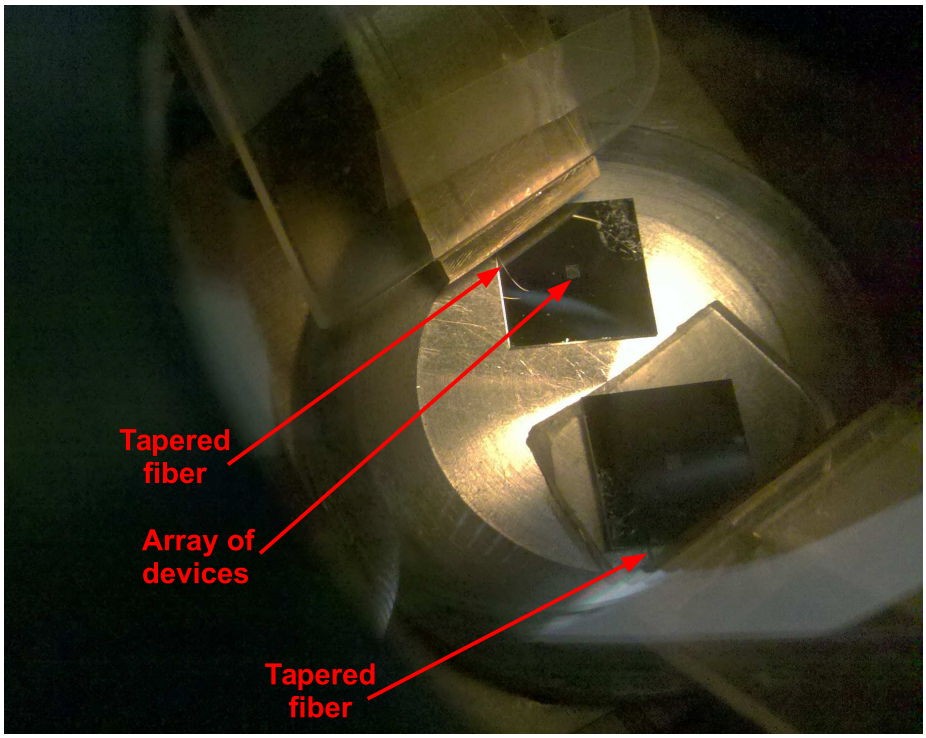

Figure B.4: Two separate tapered fibers are used within the same vacuum chamber, as shown above.

B.6 Experimental setup

Alhtough the master and slave oscillators are separated by an optical path of 3.2 km, due to practical considerations, they are located in the same vacuum chamber (Fig. B.4). However, the two oscillators are probed by independent tapered fibers, which are coupled to optical fibers running through hermetic feedthroughs to the outside. A 3.2km optical fiber delay spool serves as a delay line.

It must also be pointed out that due to variations of mechanical frequencies in the fabrication process, we use two OMOs located on the same chip. This is because typical variation between OMOs on different chips is too large for locking to be possible with the amount of gain available in the setup.

APPENDIX C

C.1 Experimental Setup and Procedure for Delay-coupled synchronisation

A more detailed schematic of experimental setup to synchronise two optomechanical oscillators (OMOs) is showin in C.1. As described in Chapter 4, each device is driven by an independent laser tuned to be blue-side of its optical resonance. The transmitted optical signals, modulated by each OMO, travel over delay line of SMF-28 optical fibres. The RF signal generated at the photodetectors (DC filters are used to block the DC signal) at the end of optical delay lines modulate the power of the lasers driving the two OMOs via electro-optic modulators (EOM). The strengths of these modulation signals are controlled by variable-gain RF amplifiers (VGA).

The coupling strengths are primarily determined by VGA1 and VGA2. The two OMOs are first pumped into self-sustained oscillations, while keeping the gain values very low (< -20 dB), so that the two devices oscillate independently. VGA1 and VGA2 are controlled by the same voltage source, and have the same gain (within their specifications) as the control-voltage is varied. The synchronisation transition i.e. when the two OMOs transition from independent oscillations at different frequencies to locked oscillations at the same frequency, is seen when the gain is increased. We increase the gain in steps of ≈ 0.9 dB.

Half of the RF oscillation signal is tapped off at each of the photodetector for analysing with an RF spectrum analyser. Since the instrument we use only has a single input channel, we analyse and record the spectrum of each oscillator independently. Therefore, each voltage scan (as described in the previous paragraph) is performed

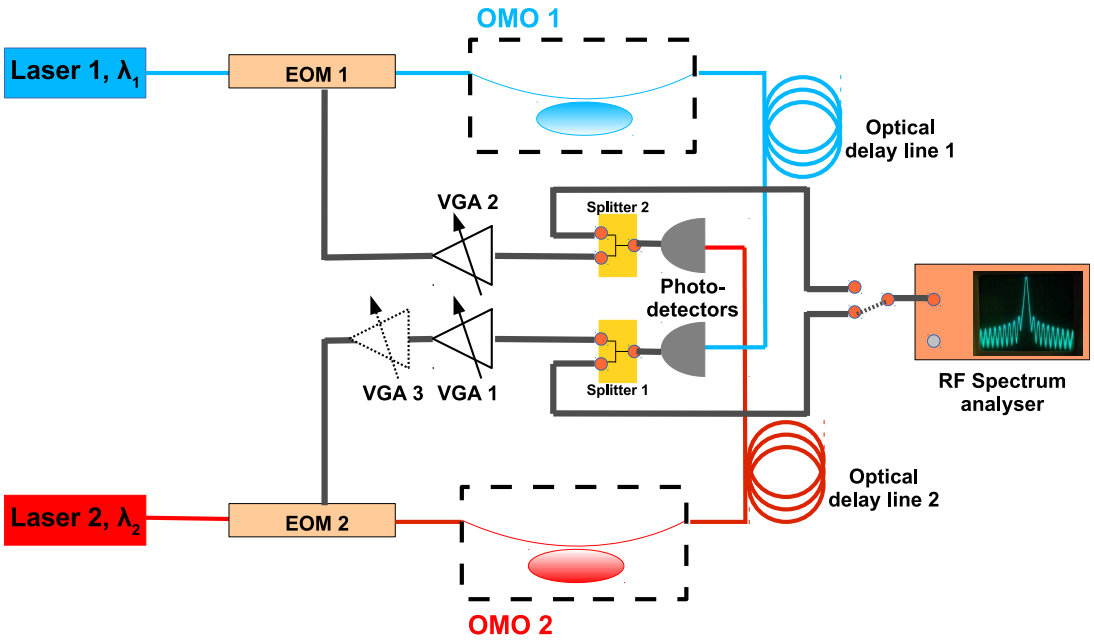

Figure C.1:

twice, first to record the output of Splitter 1 and then to record the output of Splitter 2. The two spectra are then mathematically added using numerical software to yield a combined RF spectrum for the two OMOs.

We showed in Chapter 3 and Appendix B that the response of an OMO to an externally injected periodic signal is highly asymmetric with respect to the detuning between the OMO and the external signal. Therefore, an OMO is more susceptible to locking by an external signal if that signal has a higher frequency than if it has a lower freuquency. This means that, in order to observe synchronisation dynamics, it is not enough to have equal values of gain (and thereby κ_{21} and κ_{12}).

A third amplifier VGA3, cascaded with VGA1 and controlled independently of VGA1 and VGA2, is used to differentiate between κ_{21} and κ_{12}. The gain of VGA3 is kept fixed throughout the voltage-scan described above. Therefore, the variety of synchronisation dynamics reported in Chapter 4 (and below) is seen by performing the

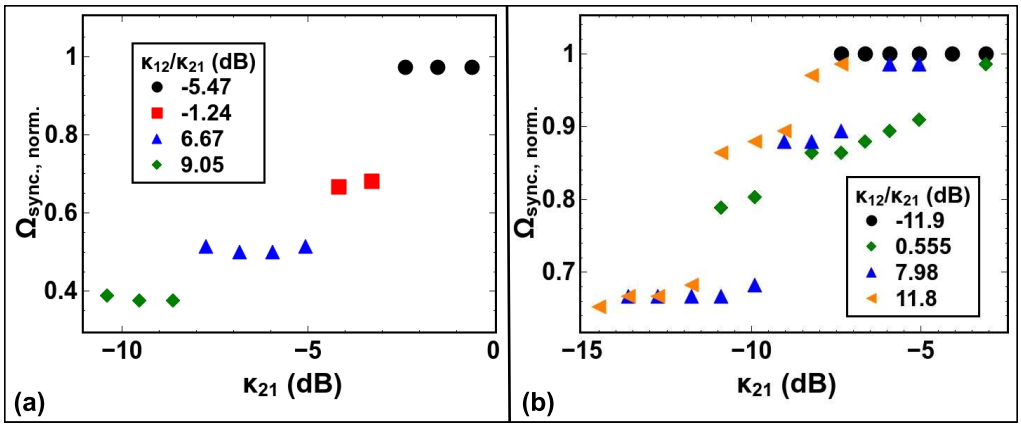

Figure C.2: **(a)** Delay = 124 ns ≈ 4× oscillation time period **(b)** Delay = 168 ns ≈ 5.5× oscillation time period

voltage scans at different values of gain supplied by VGA3.

C.2 Behaviour at different values of coupling delay

In Chapter 4, we showed that for a delay of 139 ns between the two OMOs, oscillating at 32.9 MHz and 32.97 MHz, there exist multiple states of synchronised oscillations in the coupled system. This behaviour is not restricted to this particular value of delay. We see multi-stable synchronised oscillations at other values of delay too (Fig. C.2), specifically at delays ≈ 94.7 ns, 109 ns, 124 ns, 139 ns, 153 ns, 168 ns (maximum delay investigated), as the length of the optical fiber delay line is changed in 3-meter increments (propagation delay of optical fiber ≈ 4.9 ns/m). The optical propagation times are calibrated using a technique analogous to optical time-domain reflectometry. A periodic pulse signal is input on the optical path using an electro-optic modulator, and detected at the other end of the fiber. We adjust the time period of the pulse train so that the input signal and output signal overlap (as observed on an oscilloscope). The time-period of the periodic-pulse-train is now equal to the optical propagation time.

Curiously, when the delay strays from these values, the two oscillators do not synchronise at all. Instead, for a delay of 119 ns ($\approx$ 3.85$\times$ oscillation time period), the frequencies of the OMOs drift away as the coupling strength is increased (Fig. C.3). In addition, there appears to be a phase-transition of the coupled system, where the RF power spectrum shows a feature similar to optical frequency combs. As the coupling strength is increased further, this comb-like state disappears and the original frequencies are seen again.

This behaviour appears analogous to that seen in other systems involving delay, where, depending on the delay, there could be a Hopf-bifurcation in the rotating-frame of the oscillator (i.e. in the slow-flow), leading to quasi-harmonic behaviour [59]. Similar quasi-harmonic motion, transduced by the optical cavity, could be responsible for the comb-like spectrum. In-depth analysis of Eq. C.5 is necessary to ascertain the mechanism leading to such dynamical behaviour.

Note : The phenomenon of original frequencies re-appearing for high coupling strengths is also seen for those cases when the two oscillators synchronise at a single frequency, as seen in Fig. C.4. In addition, we also see the coupled system showing aperiodic behaviour for a range of coupling strengths. This may be a signature of chaos, but this can only be confirmed by detailed mathematical analysis.

C.3 Hysteresis

The system of coupled OMOs also shows evidence of hysteresis as the coupling-strength is varied (Fig. C.5) around the synchronisation transition. Such behaviour is typically indicative of the dynamical properties of the oscillators and the nature of their coupling [77] and it may help in further analysis of Eq. C.5.

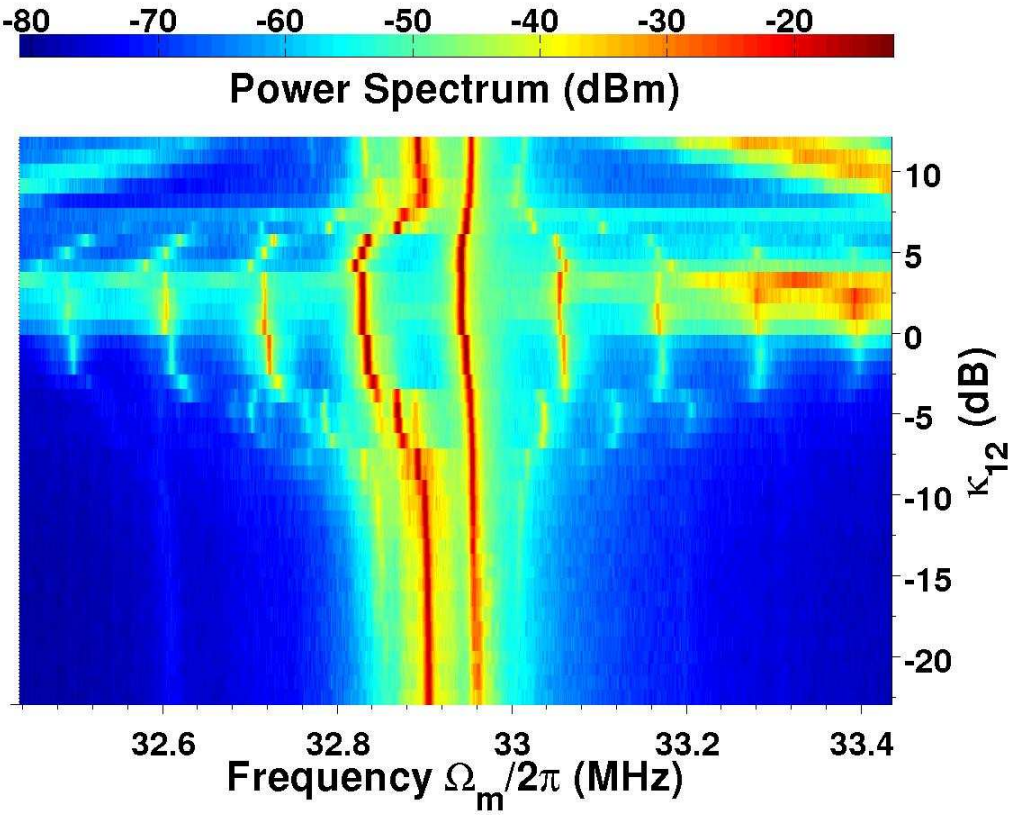

Figure C.3: For a delay of 119 ns, we see quasi-harmonic behaviour in the coupled system instead of a distinct frequency commonly associated with synchronisation. Above : κ_{12}/κ_{21} = 12.4 dB

C.4 Mathematical model for delayed coupling

As described in Appendix B, each OMO can be modelled as a pair of parametrically coupled optical and mechanical resonators (Eqs. C.1, C.2). The parameters in these equations are described in Appendix B.

$$\frac{da}{dt} = i(\Delta_0 - G_{\mathrm{om}}x)a - \Gamma_{opt}a + \sqrt{2\Gamma_{ex}}s \tag{C.1}$$

$$\frac{d^2x}{dt^2} + \Gamma_m\frac{dx}{dt} + \Omega_m^2 x = \frac{G_{\mathrm{om}}|a|^2}{m_{eff}\omega} \tag{C.2}$$

For the OMOs that we used in this demonstration of synchronisation, the optical

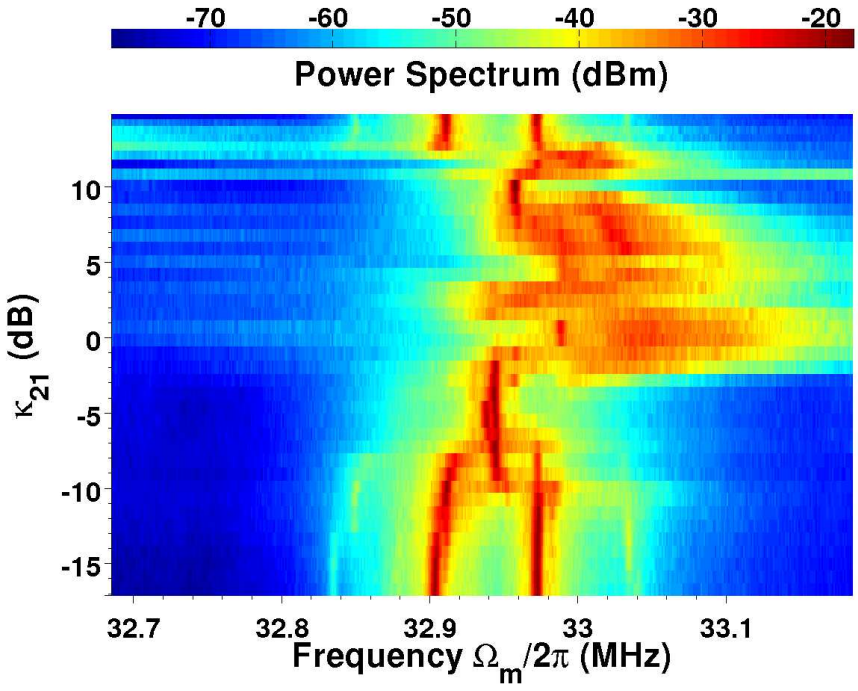

Figure C.4: Delay = 109 ns, κ_{12}/κ_{21} = 3.6 dB. De-synchronisation is seen around $\kappa_{21} \approx 13$ dB. Aperiodic behaviour is seen for $\kappa_{21} \approx 1$ dB - 9 dB

decay rate Γ_{opt} is much larger than the mechanical frequency Ω_m, and Eqs. C.1, C.2 can be approximated by a single equation Eq. C.3, where $|s|^2$ is the power of the laser driving the device.

$$\frac{d^2x(t)}{dt^2} + \Gamma_m \frac{dx(t)}{dt} + \Omega_m^2 x(t) = \frac{2G_{\mathrm{om}}\Gamma_{ex}}{m_{eff}\omega} \frac{1}{(\Delta_0 - G_{\mathrm{om}}x(t-\tau))^2 + \Gamma_{opt}^2} |s|^2 \tag{C.3}$$

The laser power $|s|^2$ driving one OMO is modulated, via an electro-optic modulator, by the RF oscillation signal of the other OMO P_{trans} Eq. C.4 (see Appendix B for details). Here, $\frac{\Gamma}{2}$ represents the strength of modulation due to P_{trans}.

$$|s|^2 = |s_0|^2(1 + \frac{\Gamma}{2}P_{trans}) \tag{C.4}$$

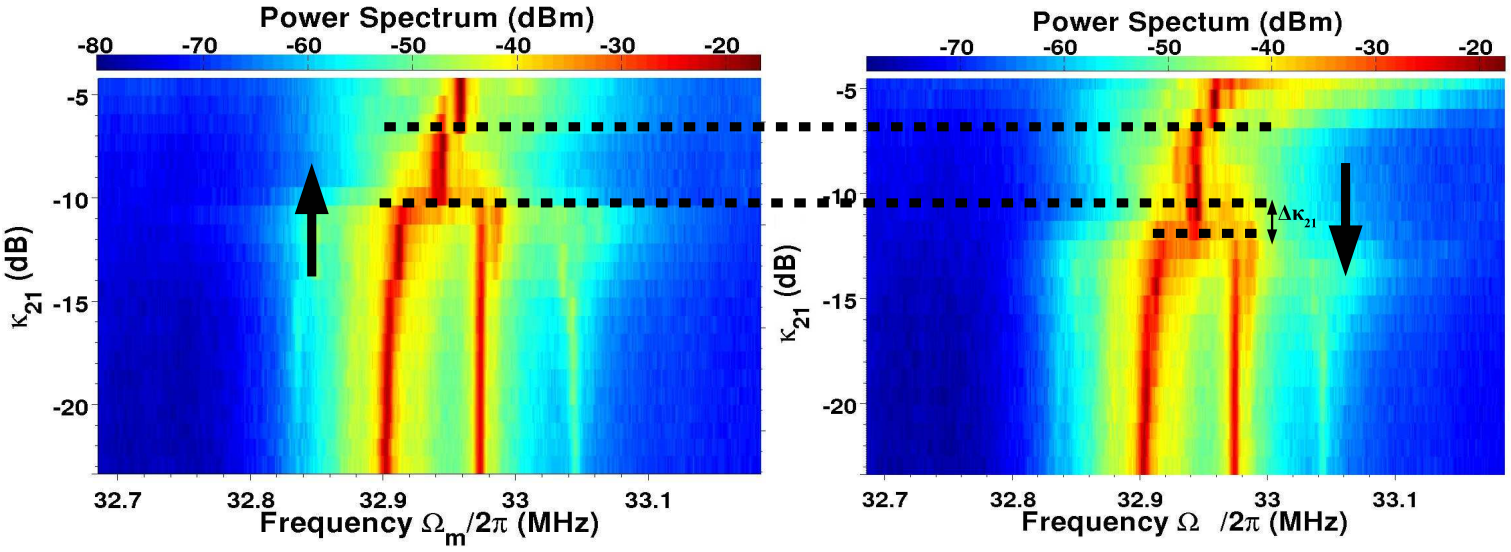

Figure C.5: Synchronisation transition for a delay of 139 ns, with $\kappa_{12}/\kappa_{21} = 6.32$ dB, as the coupling-strength is increased (left) and decreased (right). The two oscillators transition from oscillating independently to oscillating synchronously (left) at a value of κ_{21} (as denoted by dotted lines) that is different from the value when they de-synchronise (right) as the coupling-strength is decreased.

P_{trans} is the RF oscillation power of the OMO, that modulates the laser power $|s|^2$. According to Eq. B.7 from Appendix B, $P_{trans}(t) \propto x_{trans}(t)$. Substituting this in Eq. C.4, and combining it with C.3, assuming that P_{trans} is delayed by T, we get Eq. C.5, which describes the delayed coupling between the two OMOs.

$$\begin{aligned} &\frac{d^2x(t)}{dt^2} + \Gamma_m \frac{dx(t)}{dt} + \Omega_m^2 x(t) = F_{opt}(x(t))(1 + \gamma x_{trans}(t-T)) \\ &\text{where, } F_{opt}(x(t)) = \frac{2G_{\text{om}}\Gamma_{ex}}{m_{eff}\omega} \frac{1}{(\Delta_0 - G_{\text{om}}x(t-\tau))^2 + \Gamma_{opt}^2} |s_0|^2 \end{aligned} \tag{C.5}$$

BIBLIOGRAPHY

[1] Milton Abramowitz and Irene A. Stegun. *Handbook of Mathematical Functions: with Formulas, Graphs, and Mathematical Tables*. Courier Dover Publications, April 2012.

[2] Robert Adler. A study of locking phenomena in oscillators. *Proceedings of the IRE*, 34(6):351–357, June 1946.

[3] Deepak K. Agrawal, Jim Woodhouse, and Ashwin A. Seshia. Observation of Locked Phase Dynamics and Enhanced Frequency Stability in Synchronized Micromechanical Oscillators. *Physical Review Letters*, 111(8):084101, August 2013.

[4] Vilson R. Almeida, Qianfan Xu, Carlos A. Barrios, and Michal Lipson. Guiding and confining light in void nanostructure. *Optics Letters*, 29(11):1209, 2004.

[5] R. W. Andrews, R. W. Peterson, T. P. Purdy, K. Cicak, R. W. Simmonds, C. A. Regal, and K. W. Lehnert. Bidirectional and efficient conversion between microwave and optical light. *Nature Physics*, 10(4):321–326, April 2014.

[6] O. Arcizet, P.-F. Cohadon, T. Briant, M. Pinard, A. Heidmann, J.-M. Mackowski, C. Michel, L. Pinard, O. Franais, and L. Rousseau. High-Sensitivity Optical Monitoring of a Micromechanical Resonator with a Quantum-Limited Optomechanical Sensor. *Physical Review Letters*, 97(13):133601, September 2006.

[7] A. M. Armani, D. K. Armani, B. Min, K. J. Vahala, and S. M. Spillane. Ultra-high-Q microcavity operation in H2o and D2o. *Applied Physics Letters*, 87(15):151118, October 2005.

[8] Andrea M. Armani, Rajan P. Kulkarni, Scott E. Fraser, Richard C. Flagan, and

Kerry J. Vahala. Label-Free, Single-Molecule Detection with Optical Microcavities. *Science*, 317(5839):783–787, August 2007.

[9] Arthur Ashkin. Optical trapping and manipulation of neutral particles using lasers. *Proceedings of the National Academy of Sciences*, 94(10):4853–4860, May 1997.

[10] T. Bagci, A. Simonsen, S. Schmid, L. G. Villanueva, E. Zeuthen, J. Appel, J. M. Taylor, A. Srensen, K. Usami, A. Schliesser, and E. S. Polzik. Optical detection of radio waves through a nanomechanical transducer. *Nature*, 507(7490):81–85, March 2014.

[11] Mahmood Bagheri, Menno Poot, Linran Fan, Florian Marquardt, and Hong X. Tang. Photonic cavity synchronization of nanomechanical oscillators. *Physical Review Letters*, 111(21):213902, November 2013.

[12] Mahmood Bagheri, Menno Poot, Mo Li, Wolfram P. H. Pernice, and Hong X. Tang. Dynamic manipulation of nanomechanical resonators in the high-amplitude regime and non-volatile mechanical memory operation. *Nature Nanotechnology*, 6(11):726–732, November 2011.

[13] Joerg Bochmann, Amit Vainsencher, David D. Awschalom, and Andrew N. Cleland. Nanomechanical coupling between microwave and optical photons. *Nature Physics*, 9(11):712–716, November 2013.

[14] W. Bogaerts, P. De Heyn, T. Van Vaerenbergh, K. De Vos, S. Kumar Selvaraja, T. Claes, P. Dumon, P. Bienstman, D. Van Thourhout, and R. Baets. Silicon microring resonators. *Laser & Photonics Reviews*, 6(1):47–73, January 2012.

[15] Robert Bogue. MEMS sensors: past, present and future. *Sensor Review*, 27(1):7–13, January 2007.

[16] Robert W. Boyd. *Nonlinear Optics*. Academic Press, May 2008.

[17] Stefano Bregni. *Synchronization of Digital Telecommunications Networks*. Wiley, 2002.

[18] Adi R. Bulsara, Visarath In, Andy Kho, Antonio Palacios, Patrick Longhini, Joe Neff, Gregory Anderson, Christopher Obra, Salvatore Baglio, and Bruno Ando. Exploiting nonlinear dynamics in a coupled-core fluxgate magnetometer. *Measurement Science and Technology*, 19(7):075203, 2008.

[19] Kevin E. Burcham, Gregory N. De Brabander, and Joseph T. Boyd. Micromachined silicon cantilever beam accelerometer incorporating an integrated optical waveguide. volume 1793, pages 12–18, 1993.

[20] Felipe Guzmn Cervantes, Lee Kumanchik, Jon Pratt, and Jacob M. Taylor. High sensitivity optomechanical reference accelerometer over 10 kHz. *Applied Physics Letters*, 104(22):221111, June 2014.

[21] Heng-Chia Chang, Xudong Cao, Umesh K. Mishra, and R.A York. Phase noise in coupled oscillators: theory and experiment. *IEEE Transactions on Microwave Theory and Techniques*, 45(5):604–615, May 1997.

[22] Heng-Chia Chang, Xudong Cao, M.J. Vaughan, Umesh K. Mishra, and R.A York. Phase noise in externally injection-locked oscillator arrays. *IEEE Transactions on Microwave Theory and Techniques*, 45(11):2035–2042, November 1997.

[23] M. Y. Choi, H. J. Kim, D. Kim, and H. Hong. Synchronization in a system of globally coupled oscillators with time delay. *Physical Review E*, 61(1):371–381, January 2000.

[24] J. Cosp, J. Madrenas, E. Alarcon, E. Vidal, and G. Villar. Synchronization of

nonlinear electronic oscillators for neural computation. *IEEE Transactions on Neural Networks*, 15(5):1315–1327, September 2004.

[25] M. C. Cross, A. Zumdieck, Ron Lifshitz, and J. L. Rogers. Synchronization by Nonlinear Frequency Pulling. *Physical Review Letters*, 93(22):224101, November 2004.

[26] Gustavo Deco, Viktor Jirsa, A. R. McIntosh, Olaf Sporns, and Rolf Ktter. Key role of coupling, delay, and noise in resting brain fluctuations. *Proceedings of the National Academy of Sciences*, 106(25):10302–10307, June 2009.

[27] Mukeshwar Dhamala, Viktor K. Jirsa, and Mingzhou Ding. Enhancement of Neural Synchrony by Time Delay. *Physical Review Letters*, 92(7):074104, February 2004.

[28] A. Dorsel, J. D. McCullen, P. Meystre, E. Vignes, and H. Walther. Optical Bistability and Mirror Confinement Induced by Radiation Pressure. *Physical Review Letters*, 51(17):1550–1553, October 1983.

[29] Matt Eichenfield, Ryan Camacho, Jasper Chan, Kerry J. Vahala, and Oskar Painter. A picogram- and nanometre-scale photonic-crystal optomechanical cavity. *Nature*, 459(7246):550–555, May 2009.

[30] Matt Eichenfield, Christopher P. Michael, Raviv Perahia, and Oskar Painter. Actuation of micro-optomechanical systems via cavity-enhanced optical dipole forces. *Nature Photonics*, 1(7):416–422, July 2007.

[31] K. Entesari and G.M. Rebeiz. A differential 4-bit 6.5-10-GHz RF MEMS tunable filter. *IEEE Transactions on Microwave Theory and Techniques*, 53(3):1103–1110, March 2005.

[32] Thomas Erneux and Johan Grasman. Limit-cycle oscillators subject to a delayed feedback. *Physical Review E*, 78(2):026209, August 2008.

[33] Xudong Fan, Ian M. White, Siyka I. Shopova, Hongying Zhu, Jonathan D. Suter, and Yuze Sun. Sensitive optical biosensors for unlabeled targets: A review. *Analytica Chimica Acta*, 620(12):8–26, July 2008.

[34] J. Fluitman and Th. Popma. Optical waveguide sensors. *Sensors and Actuators*, 10(1):25–46, September 1986.

[35] King Y. Fong, Wolfram H.P. Pernice, Mo Li, and Hong X. Tang. Tunable optical coupler controlled by optical gradient forces. *Optics Express*, 19(16):15098, August 2011.

[36] King Yan Fong, Linran Fan, Liang Jiang, Xu Han, and Hong X. Tang. Microwave-assisted coherent and nonlinear control in cavity piezo-optomechanical systems. *Physical Review A*, 90(5):051801, November 2014.

[37] Oliver Gerberding, Felipe Guzman Cervantes, John Melcher, Jon R. Pratt, and Jacob M. Taylor. Optomechanical reference accelerometer. *arXiv:1504.01055 [physics]*, April 2015. arXiv: 1504.01055.

[38] Y Hadjar, P. F Cohadon, C. G Aminoff, M Pinard, and A Heidmann. High-sensitivity optical measurement of mechanical Brownian motion. *Europhysics Letters (EPL)*, 47(5):545–551, September 1999.

[39] Hermann A. Haus. *Waves and fields in optoelectronics*. Prentice Hall, Incorporated, 1984.

[40] Eugene Hecht. *Optics*. Pearson Education, July 2015.

[41] Georg Heinrich, Max Ludwig, Jiang Qian, Bjrn Kubala, and Florian Marquardt. Collective dynamics in optomechanical arrays. *Physical Review Letters*, 107(4):043603, July 2011.

[42] C. A. Holmes, C. P. Meaney, and G. J. Milburn. Synchronization of many nanomechanical resonators coupled via a common cavity field. *Physical Review E*, 85(6):066203, June 2012.

[43] F.C. Hoppensteadt and E.M. Izhikevich. Synchronization of MEMS resonators and mechanical neurocomputing. *IEEE Transactions on Circuits and Systems I: Fundamental Theory and Applications*, 48(2):133–138, February 2001.

[44] M. Hossein-Zadeh and K.J. Vahala. Photonic RF Down-Converter Based on Optomechanical Oscillation. *IEEE Photonics Technology Letters*, 20(4):234–236, February 2008.

[45] Mani Hossein-Zadeh and Kerry J. Vahala. Observation of injection locking in an optomechanical rf oscillator. *Applied Physics Letters*, 93(19):191115, November 2008.

[46] Roger T. Howe. Surface micromachining for microsensors and microactuators. *Journal of Vacuum Science & Technology B*, 6(6):1809–1813, November 1988.

[47] Visarath In, A. Kho, A.R. Bulsara, J.D. Neff, Salvatore Baglio, V. Sacco, Antonio Palacios, and P. Longhini. Coupling nonlinear sensors for enhanced sensitivity: a prototype using the 3 coupled-core fluxgate magnetometer. In *2005 IEEE Sensors*, pages 4 pp.–, October 2005.

[48] Visarath In, Patrick Longhini, Norman Liu, Andy Kho, Joseph D. Neff, Antonio Palacios, and Adi R. Bulsara. A bistable microelectronic circuit for sensing ex-

tremely low electric field. *Journal of Applied Physics*, 107(1):014506, January 2010.

[49] Visarath In, Antonio Palacios, Yong Ko, and Adi R. Bulsara. Coupled nonlinear sensor system for sensing a time-dependent target signal and method of assembling the system, May 2009. U.S. Classification 324/326, 324/207.16, 324/253; International Classification G01R33/04, G01B3/08; Cooperative Classification G01R33/04; European Classification G01R33/04.

[50] C. Joshi, J. Larson, M. Jonson, E. Andersson, and P. hberg. Entanglement of distant optomechanical systems. *Physical Review A*, 85(3):033805, March 2012.

[51] Stuart Kauffman and John J. Wille. The mitotic oscillator in Physarum polycephalum. *Journal of Theoretical Biology*, 55(1):47–93, November 1975.

[52] Seunghwan Kim, Seon Hee Park, and C. S. Ryu. Multistability in Coupled Oscillator Systems with Time Delay. *Physical Review Letters*, 79(15):2911–2914, October 1997.

[53] T. J. Kippenberg, S. M. Spillane, and K. J. Vahala. Modal coupling in traveling-wave resonators. *Optics Letters*, 27(19):1669–1671, October 2002.

[54] T. J. Kippenberg and K. J. Vahala. Cavity Optomechanics: Back-Action at the Mesoscale. *Science*, 321(5893):1172–1176, August 2008.

[55] Tobias J. Kippenberg and Kerry J. Vahala. Cavity opto-mechanics. *Optics Express*, 15(25):17172–17205, December 2007.

[56] Alexander G. Krause, Martin Winger, Tim D. Blasius, Qiang Lin, and Oskar Painter. A high-resolution microchip optomechanical accelerometer. *Nature Photonics*, 6(11):768–772, November 2012.

[57] U. Krishnamoorthy, R. H. Olsson III, G. R. Bogart, M. S. Baker, D. W. Carr, T. P. Swiler, and P. J. Clews. In-plane MEMS-based nano-g accelerometer with sub-wavelength optical resonant sensor. *Sensors and Actuators A: Physical*, 145146:283–290, July 2008.

[58] K. Kurokawa. Noise in synchronized oscillators. *IEEE Transactions on Microwave Theory and Techniques*, 16(4):234–240, April 1968.

[59] Lauren Lazarus, Matthew Davidow, and Richard Rand. Dynamics of an oscillator with delay parametric excitation. *International Journal of Non-Linear Mechanics*, 78:66–71, January 2016.

[60] Minho Lee, Akira Hirose, Zeng-Guang Hou, and Rhee Man Kil. *Neural Information Processing: 20th International Conference, ICONIP 2013, Daegu, Korea, November 3-7, 2013. Proceedings*. Springer, October 2013.

[61] S. Lettieri, F. Gesuele, P. Maddalena, M. Liscidini, L. C. Andreani, C. Ricciardi, V. Ballarini, and F. Giorgis. Second-harmonic generation in hydrogenated amorphous-Si1xNx doubly resonant microcavities with periodic dielectric mirrors. *Applied Physics Letters*, 87(19):191110, November 2005.

[62] G. Len Aveleyra, C. A. Holmes, and G. J. Milburn. Synchronization in a mechanical resonator array coupled quadratically to a common electromagnetic field mode. *Physical Review E*, 89(6):062912, June 2014.

[63] Fenfei Liu, Seyedhamidreza Alaie, Zayd C. Leseman, and Mani Hossein-Zadeh. Sub-pg mass sensing and measurement with an optomechanical oscillator. *Optics Express*, 21(17):19555, August 2013.

[64] Xingsheng Luan, Yongjun Huang, Ying Li, James F. McMillan, Jiangjun Zheng, Shu-Wei Huang, Pin-Chun Hsieh, Tingyi Gu, Di Wang, Archita Hati, David A.

Howe, Guangjun Wen, Mingbin Yu, Guoqiang Lo, Dim-Lee Kwong, and Chee Wei Wong. An integrated low phase noise radiation-pressure-driven optomechanical oscillator chipset. *Scientific Reports*, 4:6842, October 2014.

[65] Max Ludwig and Florian Marquardt. Quantum many-body dynamics in optomechanical arrays. *Physical Review Letters*, 111(7):073603, August 2013.

[66] Kevin Luke, Avik Dutt, Carl B. Poitras, and Michal Lipson. Overcoming Si_3n_4 film stress limitations for high quality factor ring resonators. *Optics Express*, 21(19):22829, September 2013.

[67] Marc J. Madou. *Fundamentals of Microfabrication: The Science of Miniaturization, Second Edition*. CRC Press, March 2002.

[68] I. Mahboob and H. Yamaguchi. Bit storage and bit flip operations in an electromechanical oscillator. *Nature Nanotechnology*, 3(5):275–279, May 2008.

[69] Florian Marquardt, J. G. E. Harris, and S. M. Girvin. Dynamical multistability induced by radiation pressure in high-finesse micromechanical optical cavities. *Physical Review Letters*, 96(10):103901, March 2006.

[70] Matthew H. Matheny, Matt Grau, Luis G. Villanueva, Rassul B. Karabalin, M.C. Cross, and Michael L. Roukes. Phase synchronization of two anharmonic nanomechanical oscillators. *Physical Review Letters*, 112(1):014101, January 2014.

[71] Lukas Novotny and Bert Hecht. *Principles of Nano-Optics*. Cambridge University Press, June 2006.

[72] Barbara A Paldus and Alexander A Kachanov. An historical overview of cavity-enhanced methods. *Canadian Journal of Physics*, 83(10):975–999, October 2005.

[73] Manoj Pandey, Richard H. Rand, and Alan T. Zehnder. Frequency locking in a forced mathieuvan der polduffing system. *Nonlinear Dynamics*, 54(1-2):3–12, October 2008.

[74] Arkady Pikovsky and Jrgen Kurths. *Synchronization: A Universal Concept in Nonlinear Sciences*. Cambridge University Press, April 2003.

[75] D. V. Ramana Reddy, A. Sen, and G. L. Johnston. Time delay induced death in coupled limit cycle oscillators. *Physical Review Letters*, 80(23):5109–5112, June 1998.

[76] R. Ramaswami. Optical fiber communication: from transmission to networking. *IEEE Communications Magazine*, 40(5):138–147, May 2002.

[77] Richard H. Rand. Lecture notes on nonlinear vibrations. Working paper, May 2012. http://hdl.handle.net/1813/28989.

[78] B. Razavi. A study of injection locking and pulling in oscillators. *IEEE Journal of Solid-State Circuits*, 39(9):1415–1424, September 2004.

[79] T.O. Rocheleau, A.J. Grine, K.E. Grutter, R.A. Schneider, N. Quack, M.C. Wu, and C.T.-C. Nguyen. Enhancement of mechanical Q for low phase noise optomechanical oscillators. In *2013 IEEE 26th International Conference on Micro Electro Mechanical Systems (MEMS)*, pages 118–121, January 2013.

[80] H. Rokhsari, T. J. Kippenberg, T. Carmon, and K. J. Vahala. Radiation-pressure-driven micro-mechanical oscillator. *Optics Express*, 13(14):5293, 2005.

[81] Hossein Rokhsari, Mani Hossein-Zadeh, Ali Hajimiri, and Kerry Vahala. Brownian noise in radiation-pressure-driven micromechanical oscillators. *Applied Physics Letters*, 89(26):261109, December 2006.

[82] Enrico Rossoni, Yonghong Chen, Mingzhou Ding, and Jianfeng Feng. Stability of synchronous oscillations in a system of Hodgkin-Huxley neurons with delayed diffusive and pulsed coupling. *Physical Review E*, 71(6):061904, June 2005.

[83] Peter R. Saulson. Thermal noise in mechanical experiments. *Physical Review D*, 42(8):2437–2445, October 1990.

[84] A. Schliesser, P. DelHaye, N. Nooshi, K. J. Vahala, and T. J. Kippenberg. Radiation Pressure Cooling of a Micromechanical Oscillator Using Dynamical Backaction. *Physical Review Letters*, 97(24):243905, December 2006.

[85] Bradley S. Schmidt, Allen H. Yang, David Erickson, and Michal Lipson. Optofluidic trapping and transport on solid core waveguides within a microfluidic device. *Optics Express*, 15(22):14322, 2007.

[86] H. G. Schuster and P. Wagner. Mutual Entrainment of Two Limit Cycle Oscillators with Time Delayed Coupling. *Progress of Theoretical Physics*, 81(5):939–945, May 1989.

[87] Ehsan Shah Hosseini, Siva Yegnanarayanan, Mohammad Soltani, and Ali Adibi. Ultra-High Quality Factor Microdisk Resonators for Chip-Scale Visible Integrated Photonics. page FMG4. OSA, 2008.

[88] Benjamin S. Sheard, Malcolm B. Gray, Conor M. Mow-Lowry, David E. McClelland, and Stanley E. Whitcomb. Observation and characterization of an optical spring. *Physical Review A*, 69(5):051801, May 2004.

[89] Nicols Sherwood-Droz and Michal Lipson. Scalable 3d dense integration of photonics on bulk silicon. *Optics Express*, 19(18):17758, August 2011.

[90] Seung-Bo Shim, Matthias Imboden, and Pritiraj Mohanty. Synchronized oscillation in coupled nanomechanical oscillators. *Science*, 316(5821):95–99, April 2007.

[91] Mohammad Soltani, Jun Lin, Robert A. Forties, James T. Inman, Summer N. Saraf, Robert M. Fulbright, Michal Lipson, and Michelle D. Wang. Nanophotonic trapping for precise manipulation of biomolecular arrays. *Nature Nanotechnology*, 9(6):448–452, June 2014.

[92] Miguel C. Soriano, Jordi Garca-Ojalvo, Claudio R. Mirasso, and Ingo Fischer. Complex photonics: Dynamics and applications of delay-coupled semiconductors lasers. *Reviews of Modern Physics*, 85(1):421–470, March 2013.

[93] K.D. Stephan. Inter-injection-locked oscillators for power combining and phased arrays. *IEEE Transactions on Microwave Theory and Techniques*, 34(10):1017–1025, October 1986.

[94] Steven Strogatz. *Sync: The Emerging Science of Spontaneous Order*. Hyperion, March 2003.

[95] Xiankai Sun, Jiangjun Zheng, Menno Poot, Chee Wei Wong, and Hong X. Tang. Femtogram Doubly Clamped Nanomechanical Resonators Embedded in a High-Q Two-Dimensional Photonic Crystal Nanocavity. *Nano Letters*, 12(5):2299–2305, May 2012.

[96] Atsuko Takamatsu. Spontaneous switching among multiple spatio-temporal patterns in three-oscillator systems constructed with oscillatory cells of true slime mold. *Physica D: Nonlinear Phenomena*, 223(2):180–188, November 2006.

[97] Atsuko Takamatsu, Teruo Fujii, and Isao Endo. Time Delay Effect in a Liv-

ing Coupled Oscillator System with the Plasmodium of \textit{Physarum polycephalum}. *Physical Review Letters*, 85(9):2026–2029, August 2000.

[98] A. Tomadin, S. Diehl, M. D. Lukin, P. Rabl, and P. Zoller. Reservoir engineering and dynamical phase transitions in optomechanical arrays. *Physical Review A*, 86(3):033821, September 2012.

[99] Scott S. Verbridge, Rob Ilic, H. G. Craighead, and Jeevak M. Parpia. Size and frequency dependent gas damping of nanomechanical resonators. *Applied Physics Letters*, 93(1):013101, July 2008.

[100] Scott S. Verbridge, Jeevak M. Parpia, Robert B. Reichenbach, Leon M. Bellan, and H. G. Craighead. High quality factor resonance at room temperature with nanostrings under high tensile stress. *Journal of Applied Physics*, 99(12):124304, June 2006.

[101] F. Vollmer, S. Arnold, and D. Keng. Single virus detection from the reactive shift of a whispering-gallery mode. *Proceedings of the National Academy of Sciences*, 105(52):20701–20704, December 2008.

[102] Gustavo S. Wiederhecker, Long Chen, Alexander Gondarenko, and Michal Lipson. Controlling photonic structures using optical forces. *Nature*, 462(7273):633–636, December 2009.

[103] Stephen Wirkus and Richard Rand. The Dynamics of Two Coupled van der Pol Oscillators with Delay Coupling. *Nonlinear Dynamics*, 30(3):205–221, November 2002.

[104] M.C. Wu, O. Solgaard, and J.E. Ford. Optical MEMS for Lightwave Communication. *Journal of Lightwave Technology*, 24(12):4433–4454, December 2006.

[105] H.-J. Wnsche, S. Bauer, J. Kreissl, O. Ushakov, N. Korneyev, F. Henneberger, E. Wille, H. Erzgrber, M. Peil, W. Elser, and I. Fischer. Synchronization of Delay-Coupled Oscillators: A Study of Semiconductor Lasers. *Physical Review Letters*, 94(16):163901, April 2005.

[106] Serhiy Yanchuk. Discretization of frequencies in delay coupled oscillators. *Physical Review E*, 72(3):036205, September 2005.

[107] Wenyan Yu, Wei C. Jiang, Qiang Lin, and and Tao Lu. Cavity optomechanical transduction sensing of single molecules. *arXiv:1504.03727 [cond-mat, physics:physics]*, April 2015. arXiv: 1504.03727.

[108] M. Zalalutdinov, K. L. Aubin, M. Pandey, A. T. Zehnder, R. H. Rand, H. G. Craighead, J. M. Parpia, and B. H. Houston. Frequency entrainment for micromechanical oscillator. *Applied Physics Letters*, 83(16):3281–3283, October 2003.

[109] K. Zandi, J.A. Belanger, and Y.-A. Peter. Design and Demonstration of an In-Plane Silicon-on-Insulator Optical MEMS Fabry-Perot-Based Accelerometer Integrated With Channel Waveguides. *Journal of Microelectromechanical Systems*, 21(6):1464–1470, December 2012.

[110] Mian Zhang, Gustavo Luiz, Shreyas Shah, Gustavo Wiederhecker, and Michal Lipson. Eliminating anchor loss in optomechanical resonators using elastic wave interference. *Applied Physics Letters*, 105(5):051904, August 2014.

[111] Mian Zhang, Shreyas Shah, Jaime Cardenas, and Michal Lipson. Synchronization and Phase Noise Reduction in Micromechanical Oscillator Arrays Coupled through Light. *Physical Review Letters*, 115(16):163902, October 2015.

[112] Mian Zhang, Gustavo S. Wiederhecker, Sasikanth Manipatruni, Arthur Barnard, Paul McEuen, and Michal Lipson. Synchronization of micromechanical oscillators using light. *Physical Review Letters*, 109(23):233906, December 2012.

[113] Jun Zou, Chang Liu, J. Schutt-Aine, Jinghong Chen, and Sung-Mo Kang. Development of a wide tuning range MEMS tunable capacitor for wireless communication systems. In *Electron Devices Meeting, 2000. IEDM '00. Technical Digest. International*, pages 403–406, December 2000.